Development of a Tunable Frequency Shift Filter Using a Praseodymium Doped Y_2SiO_5-crystal

Yupan Bao
Supervisor: Qian Li
Co-supervisor: Stefan Kröll

Master's Thesis
January, 2016

LUND
UNIVERSITY

Department of Physics
Atomic Physics Division

Abstract

In this thesis, a tunable frequency shift filter (FSF) with a $1 \sim 2$ MHz passband created in a praseodymium doped Y_2SiO_5-crystal using a special hole burning technique is developed and tested. The FSF is able to shift the frequency of its passband and the light passing through the passband by applying an external electric field, where the frequency shift is proportional to the applied field. Since most of the current frequency shift techniques require the light to be sent in at certain angles (a specific special mode) to the shifter, the 2π acceptance angle for light of this FSF makes it unique and work more efficiently and less restrictively. The FSF can also slow down the group velocity of the light pulse passing through its passband at the order of 10^4 to 10^5. The result of the experimental test of the FSF is quite good. For the FSF with a $1 \sim 2$ MHz passband, the light is slowed down to $c/10^4 \sim c/10^5$. For a 1 MHz FSF, the frequency shift of $-4 \sim 4$ MHz for both the passband and the light pulse is achieved. The switch-on time for the FSF is around 200 ns limited by the rise time of the electric field.

Popular Science

When you look upon the sky enjoying the beautiful aurora in north of Sweden, are you curious what is happening over there? When you go through the security check and have you luggage scanned, do you wonder how the image is shown? It is all about the light-matter interaction! When light meets matter, happens the story. Different stories happen for different matters, and people are using these stories for different purposes. The story (interaction) happening in this project is between light and rare earth ions that doped in a crystal.

When light passes through the crystal, it will be absorbed (the story will happen) if the frequency of the light coincides with the transition of the rare earth ion (if the light meets the right matter). A bandpass filter will absorb all light within a certain frequency range except for light having the same frequency as its passband. So light with the frequency different from the passband will be filtered out when passing through the filter. This project is about to create a special spectral filter with praseodymium doped Y_2SiO_5-crystal using the hole burning technique. How is that? Simply speaking, the light with the frequency equal to the passband is pre-sent into the crystal to interact with the 'right ions'. After the interaction, all the 'right ions' will be burnt away, so when the light having the same frequency as the passband comes, there will be no 'right ions' for it to interact with, thus no absorption will happen.

Why do we create such a filter and what is interesting for this filter? Well, with this filter, we could slow down the speed of the light passing in the passband for the order of 10^4 to 10^5! Moreover, by applying an external electric field, the frequency of the passband and the light passing in the passband could be shifted with the frequency shift proportional to the magnitude of the electric field.

Acknowledgements

Firstly, I would like to thank my supervisor Qian Li for her constant help and patient explanations during the lab and thesis writing. There was a time I lost all my motivation to work, it was your encouragement and supportive smile that inspired me back. Without you, I could not imagine how can I possibly finish this project.

I would also like to thank my co-supervisor Stefan Kröll for giving me the opportunity to take on this interesting project. Thank you for always being supportive and concerned and taking time to answer my questions.

The quantum information group has a very friendly and warm working environment. It was Stefan and Lar's enthusiasm about science that attracted me to the group at the first place and inspired me during the whole project. The smiles from and friendly chatting with everyone made the time here so enjoyable. I would like to thank and give me best wishes to all current and former members of the group.

Thanks also go to Mariusz Graczyk and Ivan Maximov from NanoLund for the gold coating of the crystal and the former Ph.D. student Mattias Nilsson for his code files.

Personally, I wish to thank all my friends in Lund who decorated my last two years with happy memories. Specially, I would like to thank Chen Guo for his patient explanations about my superficial laser questions and rescuing me in raining night when I accidentally locked myself outside the office. Special thanks also go to Rickard Lydahl for helping me to correct the English of the thesis and the wonderful time we spent together during the lectures, tutorials and lunch.

Finally, I would like to thank my parents for their love and unending support. Being your daughter is the luckiest thing that ever happened to me. Lastly but not least importantly, to my beloved one and best friend, Taoyan Xiong, thank you for your love and companion during both the hardest and happiest days.

ABBREVIATIONS

FSF-	Frequency Shift Filter
UOT-	Ultrasound Optical Tomography
PC-	Phase Conjugator
REE-	Rare-earth Element
IUPAC-	International Union of Pure and Applied Chemistry
BS-	Beam Splitter
PD-	Photo Detector
FFT-	Fast Fourier Transform
FS-	Frequency shifter

Contents

1 Introduction

In this thesis, a tunable frequency shift filter (FSF) created in a praseodymium doped Y_2SiO_5-crystal using the hole burning technique with a $1 \sim 2$ MHz passband and a 2π acceptance angle for the light is developed and tested. As indicated by its name, the frequency of the passband and the light that passes through the passband can be shifted by applying an electric field, where the frequency shift is proportional to the applied field.

This FSF provides a new approach to shift the frequency of the light with a 2π acceptance angle for the light. While most of the current frequency shift techniques require the light to be sent in at a certain angle (a specific special mode) to the shifter, the 2π acceptance angle of the FSF makes it unique and can be used less restrictively and more efficiently.

The development of such a filter is initially motivated by the ultrasound optical tomography (UOT) technique, a biological imaging method that combines the high contrast of optical imaging and the high resolution of ultrasound imaging. For tissue deep inside the body, no current technique can provide such good imaging. UOT is thus very promising for medical treatment and diagnostics. Although having been proposed in 1993 [1], it has not been put into practical use yet. Recently, an optimised UOT using a slow light effect occurred in the spectral filter based on rare-earth-ion doped crystal is proposed [2], where the FSF is a crucial part. This new imaging method combined with the slow light and UOT can also be applied in many other fields to provide imagines of diffuse materials, such as clouding images and underwater imaging [3].

The spectral profile of such a FSF is proposed and the task of this thesis is to create such a structure using the spectral hole-burning technique and test the performance of the FSF experimentally. The simulation of the structure creation is given by an existing *Matlab* code created by former Ph.D. student using a population distribution model. Since the electric field is applied for the structure creation, the code is modified by the author so that the electric field could be added in the simulation. The homogeneity of the electric field applied on the crystal is analysed and simulated by *Comsol* [4]. The experiment is conducted in the lab of the *Quantum Information* group in Atomic Physics Department of Lund Univeristy lead by Stefan Kröll together with the supervisor Qian Li. The result of the experiment turns out to be very satisfactory. For the FSF with a $1 \sim 2$ MHz passband, the light can be slowed down to $c/10^4 \sim c/10^5$. And the frequency shift of $-4 \sim 4$ MHz for both the passband and the light pulse are achieved for a 1 MHz FSF with the switch-on time around 200 ns. The result will be published by the group in the future.

However, although the frequency-shifted light pulse can be clearly observed, the quantitative efficiency of the FSF is not measured. Moreover, as discussed in the Outlook, it is possible to create a larger FSF using a similar creation method. It is not tested due to the limitation of the voltage supply.

The thesis is written in following structure: the theoretical knowledge concerning this FSF is discussed in Sec.2-4 within the knowledge scope of the author; the FSF including its structure, creation and simulation is discussed in Sec.5; the experiment and the results testing the FSF is given in Sec.6; the UOT will be discussed in Sec.7; and finally the conclusion and some outlook are discussed in Sec.8.

2 Rare-earth-ion-doped crystal: Praseodymium in Y_2SiO_5

The Rare-earth-ion-doped crystal $Pr^{3+} : Y_2SiO_5$ is used in this project because of its superior properties, *i.e.* the long coherence time and long-lived hyperfine levels of the 4f-4f transition of Pr ion, for creating a high performance slow light spectral filter. Its general chemical properties, spectroscopic properties, *i.e.* the energy levels and line profile, and the crystal properties, *i.e.* the crystal structure and the dipole moment orientations, will be discussed in this section.

2.1 Chemical properties of Rare-earth-elements

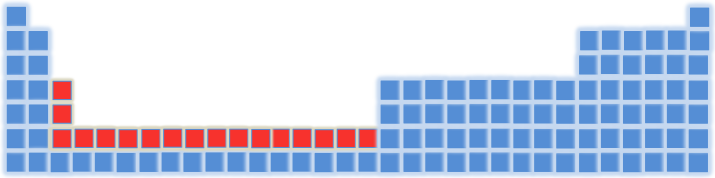

Figure 1: REE (marked red) in periodic table.

The rare-earth elements (REE), according to the definition by International Union of Pure and Applied Chemistry (IUPAC), include Scandium, Yttrium and the fifteen *Lanthanides* (originally come from the Greek word $\boldsymbol{\lambda\alpha\nu\theta\alpha\nu\varepsilon\iota\nu}$ meaning "to lie hidden") as shown in the periodic table in Fig.1. Although named 'rare', REE are quite plentiful in Earth's crust: even the least abundant REE (Lutetium) is nearly 200 times richer than gold. They are referred as 'rare' mainly because of their little tendency of being found concentrated in exploitable ore deposits [5].

When doped into inorganic crystals, REE tends to become triply charged. The trivalent *Lanthanides* shares the configuration of $[Xe]4f^n$, with a xenon core having the configuration of $1s^2 2s^2 2p^6 3s^2 3p^6 4s^2 3d^{10} 4p^6 5s^2 4d^{10} 5p^6$ and n valence electrons in the 4f-subshell.

2.2 Spectroscopic properties of Praseodymium in a Y_2SiO_5-crystal

The spectroscopic properties of a praseodymium-doped Y_2SiO_5-crystal that are important for this project, *i.e.* energy levels, line profile, will be discussed in this section.

2.2.1 Energy levels

For trivalent Praseodymium (Pr^{3+}), it has two valence electrons in the 4f-subshell. Since the 4f-subshell is shielded from the environment by the two outer fulfilling subshells 5s and 5p [6], the energy levels of Pr^{3+} can be treated as an atom with the perturbations from the crystal environment. Within the scope of this approximation, the fine structure energy levels of Pr^{3+} 'atom' can be presented as ${}^{2S+1}L_J$, where S, L and J are the total electron spin, total orbital angular momentum and total angular momentum of the two valence electrons respectively. These levels will be split into at most $2J+1$ *Stark levels* by the electrostatic crystal field. The material of the crystal and its symmetry properties have great influence on the energy levels of the ion, thus the Pr ions doped in different crystallogrphical sites have different spectra. The transition ${}^3H_4 \leftrightarrow {}^1D_2$ (605.977 nm)

that has been used in this project comes from the Pr ions doped in *site I*. The energy levels of $^1D_2$ state and $^3H_4$ state of Pr ion are listed in Table 1.

Table 1: The relevant energy levels for 0.02% $Pr^{3+} : Y_2SiO_5$ at *site I* [7]. The data was acquired at 1.4 **K** and four energy levels of $^3H_4$ around 250 cm^{-1} were not resolved in the spectrum.

	Energy $[cm^{-1}]$		Energy $[cm^{-1}]$
$^3H_4$	0	$^1D_2$	16502
	88		16561
	146		16723
	∼250		17001
	∼250		17297
	∼250		/
	∼250		
	758		
	880		

2.2.2 Hyperfine structure

The hyperfine structure of an ion is induced by the interaction between the nuclear magnetic and electric moments together with the electronic shell. For Praseodymium, who has only one naturally abundant isotope (^{141}Pr) with nuclear spin $I = 5/2$, its hyperfine structure is mainly caused by the second order hyperfine interaction and the electric quadrupole interaction [8]. Without any external magnetic field, the lowest crystal field state of $^1D_2$ and $^3H_4$ will be split into three doubly degenerate hyperfine levels with nuclear magnetic quantum numbers $m_I = \pm 5/2,\ \pm 3/2$, and $\pm 1/2$ as shown in Fig.2.

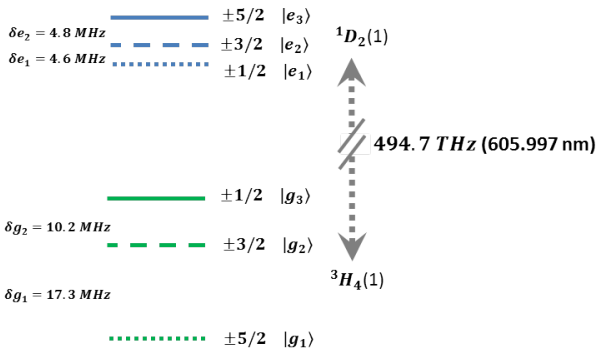

Figure 2: The hyperfine splitting of the ground and excited states are given as δg_1, δg_2, δe_1 and δe_2. Every sublevel is presented with its nuclear magnetic quantum numbers m_I and denotation, *e.g.* $|e_1\rangle$, $|g_1\rangle$. The data is taken from *Ref* [7] at 1.4 **K** for 0.02% $Pr^{3+} : Y_2SiO_5$ at *site I*.

2.2.3 Spectral broadening

The broadening of a spectral line has two mechanisms: the homogeneous broadening due to the intrinsic properties of certain ion and the inhomogeneous broadening due to the different extrinsic environment of different ions.

Homogeneous linewidth The homogeneous linewidth, Γ_h, comes from two mechanisms:

$$\Gamma_h = \Gamma_\tau + \Gamma_{dephasing}. \tag{1}$$

The Γ_τ, the ultimate limit of the homogeneous linewidth, comes from the finite nature of the lifetime of the excited state due to the uncertainty principle between energy and time. The spectral line of an exponential decay with lifetime T_1 will be Lorentzian-shaped with linewidth

$$\Gamma_\tau = \frac{1}{2\pi T_1}, \tag{2}$$

according to the Fourier transform. Moreover, since the spectra normally come from more than one ion, the dephasing process will broaden the linewidth as well. The main contributions for the dephasing process are:

$$\Gamma_{dephasing} = \Gamma_{phon} + \Gamma_{field} + \Gamma_{ISD}, \tag{3}$$

where Γ_{phon} is the contribution from the phonon scattering which is the dominating process at high temperature, Γ_{field} is the contribution from the random changes of the crystal field caused by the flip of the host ions and Γ_{ISD} is the contribution from the changes in the local environment due to the excitation or population relaxation of other ions in the crystal (so-called instantaneous spectral diffusion) [7, 9].

The homogeneous linewidth is usually associated to the coherence time T_2 of the ion by

$$\Gamma_h = \frac{1}{\pi T_2}. \tag{4}$$

Consequently, the coherence time T_2 is limited by the lifetime T_1 by $T_2 \leq 2T_1$. The T_1 and T_2 of the ${}^3H_4(1) \leftrightarrow {}^1D_2(1)$ of $Pr^{3+} : Y_2SiO_5$ in *site I* at 1.4 **K** are listed in Table 2.

Table 2: Some spectral and relaxation parameters for the ${}^3H_4(1) \leftrightarrow {}^1D_2(1)$ of 0.02% $Pr^{3+} : Y_2SiO_5$ in *site I* at 1.4 **K**[7].

T_1	$164 \pm 5\ \mu s$
T_2	$152\ \mu s$
Γ_τ	$970 \pm 20\ Hz$
Γ_{ih}	$4.4\ GHz$

At liquid helium temperature, the homogeneous linewidth is very small, which means that every individual ion can only interact with light within a narrow frequency range. This feature is appreciated in the spectral hole-burning technique as discussed in Sec.4.

Inhomogeneous linewidth For a REE-doped crystal, the ions are surrounded by slightly different crystal environment, *e.g.* from the crystal strain discussed in Sec.2.3.1. The energy levels and transition frequencies of each ion will therefore differ slightly from each other. The resultant absorption line will be broadened as shown in Fig.3. This is the so-called *inhomogeneous broadening* and the inhomogeneous linewidth, Γ_{ih}, of $Pr^{3+} : Y_2SiO_5$ with low dopant is a few GHz.

The inhomogeneous broadening becomes dominating at liquid helium temperature (Γ_{ih}/Γ_h can be as large as 10^7-10^8 [10]). The Γ_h and Γ_{ih} of ${}^3H_4(1) \leftrightarrow {}^1D_2(1)$ of $Pr^{3+} : Y_2SiO_5$ in *site I* at 1.4 **K** is listed in Table 2.

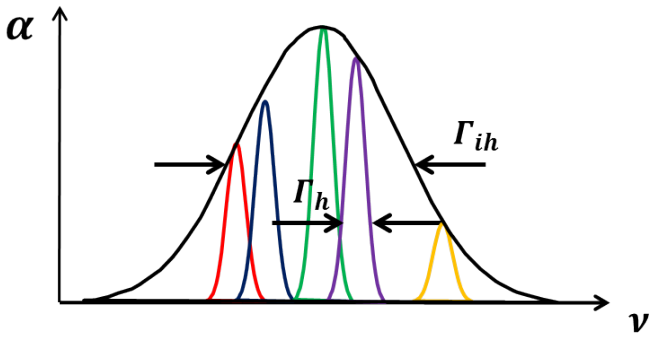

Figure 3: The inhomogeneous broadening of the spectra. The transition of different ions is shifted because of the different crystal environment. As a result, the inhomogeneous linewidth is much larger than the homogeneous linewidth.

2.3 The Y_2SiO_5-crystal

2.3.1 The crystal structure

In crystallography, a crystal is classified into different crystal systems by its lattice structure which is defined by the lengths of the cell edges (a, b, c) and the angles between them (α, β, γ) as shown in Fig.4a. One of the popular crystal hosts for REE material, the *Yttrium silicate* (Y_2SiO_5), used for this project belongs to the monoclinic crystal system. Here the lattice has three inequivalent edge-lengths and only one non-orthogonal angle β (the angle between a and c). The monoclinic cell of Y_2SiO_5-crystal is described by $a = 1.041$ nm, $b = 0.6726$ nm, $c = 1.249$ nm and $\beta = 102.65°$ [11].

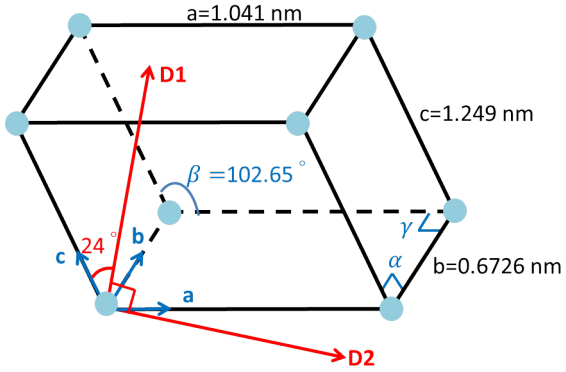

(a) The crystal lattice structure and principle axe (D_1, D_2 and b) of Y_2SiO_5-crystal.

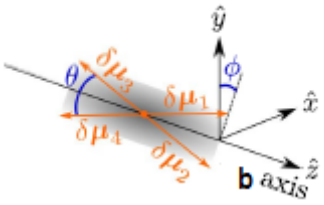

(b) The four orientations lay symmetrically along b axis with the angle $\theta = 24.8°$ and $\phi \sim 35°$ [12], figure is taken from the same reference.

Figure 4: Crystal structure and dipole orientations of Y_2SiO_5-crystal.

Because of the biaxiality, the optical principal axes do not coincide with the crystal axes except for the b axis. The other two principal axes labelled as D_1 and D_2 lie in the a-c plane with D_1 being 79° from the a axis and 24° from the c axis as shown in Fig.4a. When doping into the crystal, the rare-earth ions will substitute the Y ions who occupy two crystallographically inequivalent sites, the so-called *site I* and *site II*. The one of interests for this project is in *site I*. Since Pr ions and Y ions have different diameters, the doping process will introduce strain in the crystal which contributes to the inhomogeneous linewidth discussed in Sec.2.2.3.

2.3.2 Dipole moment orientation

When applying a direct current electric field $\mathbf{E}$ on the crystal, the ${}^3H_4(1) \leftrightarrow {}^1D_2(1)$ transition will experience a linear Stark shift because of the difference of the electric dipole moment between the two states. The Stark shift, Ω_E, is given by

$$\Omega_E = \frac{\delta\boldsymbol{\mu} \cdot \boldsymbol{E}}{\hbar}, \tag{5}$$

where $\delta\boldsymbol{\mu} = \boldsymbol{\mu}_g - \boldsymbol{\mu}_e$ is the difference between the static dipole moments of ground and excited states, which will be referred as *dipole moment* in the remaining thesis. The dipole moment for $Pr^{3+} : Y_2SiO_5$ in *site I* has the magnitude of 111.6 kHz/(V$\cdot$ cm^{-1}) [12] measured by photon echo method and four possible orientations who lie on the same plane and are symmetric along b axis as demonstrated in Fig.4b.

3 Light-matter interaction

In this project, the light is used to transfer ions between different energy states and it is, in turn, manipulated by being absorbed, scattered or emitted by the ions. Since the Pr^{3+} ion can be treated as an atom, as discussed in Sec.2.2.1, and the ${}^3H_4(1) \leftrightarrow {}^1D_2(1)$ transition only concerns with two energy levels, the Pr^{3+} ion will be approximated by an atom with a two-level system perturbed by an oscillating electric field. This *semiclassical* treatment, where the light is treated as a classical electric field while the atom is quantized, will be discussed in Sec.3.1. The light, however, will be studied as a plane electromagnetic wave propagating in a dispersive medium in the Sec.3.2. Finally, the so-called *slow light effect* will be discussed in Sec.3.3.

3.1 Two-level atom perturbed by electromagnetic radiation

3.1.1 The two-level system

In quantum mechanics, a two-level atom is described by the wavefunction solving from the Schrödinger equation $i\hbar\frac{\partial \mathbf{\Psi}}{\partial t} = H\mathbf{\Psi}$ as

$$|\psi(t)\rangle = c_g(t)|g\rangle + c_e(t)|e\rangle e^{-i\omega_{ge}t}, \tag{6}$$

where $\omega_{ge} = \omega_g - \omega_e = \frac{(E_g - E_e)}{\hbar}$ is the resonance frequency of the atomic transition, $c_g(t)$ and $c_e(t)$ are the probability coefficients of the two states with the normalisation requirements:

$$|c_g(t)|^2 + |c_e(t)|^2 = 1. \tag{7}$$

3.1.2 Interaction with electromagnetic radiation

The monochromatic and linearly polarised light can be classically treated as an oscillating electric field as

$$\boldsymbol{E}(t) = E_0(t) \cdot \hat{\boldsymbol{e}} \cos(\omega t), \tag{8}$$

The interaction of such radiation with the atom produces a perturbation in the Hamiltonian H as

$$H_I(t) = -\boldsymbol{\mu_{ge}} \cdot \boldsymbol{E}(t), \tag{9}$$

where $\boldsymbol{\mu_{ge}} = -e\langle g|\mathbf{r}|e\rangle$ is the transition dipole moment between the two levels. Solving the Schrödinger equation with the perturbation leads to

$$i\dot{c_g} = c_e\{e^{i(\omega-\omega_{ge})t} + e^{-i(\omega+\omega_{ge})t}\}\frac{\Omega}{2}, \tag{10}$$

$$i\dot{c_e} = c_g\{e^{i(\omega+\omega_{ge})t} + e^{-i(\omega-\omega_{ge})t}\}\frac{\Omega^*}{2}, \tag{11}$$

where

$$\Omega = \frac{\boldsymbol{E} \cdot \boldsymbol{\mu_{ge}}}{\hbar}, \tag{12}$$

and the dot over c_g and c_e defines the time derivative of the respective variables. Since the term with $(\omega + \omega_{ge})t$ oscillates rapidly and therefore will average to zero over any practical interaction time, Eq.10 and Eq.11 can be approximated as

$$i\dot{c_g} = c_e e^{i(\omega-\omega_{ge})t}\frac{\Omega}{2}, \tag{13}$$

$$i\dot{c_e} = c_g e^{-i(\omega-\omega_{ge})t}\frac{\Omega^*}{2}. \tag{14}$$

Given the initial conditions of being in the ground state as $c_g(0) = 1$ and $c_e(0) = 0$, the two probability coefficients will be solved as

$$|c_e(t)|^2 = \frac{\Omega^2}{W^2} sin^2(\frac{Wt}{2}), \tag{15}$$

$$|c_g(t)|^2 = 1 - \frac{\Omega^2}{W^2} sin^2(\frac{Wt}{2}), \tag{16}$$

with

$$W^2 = \Omega^2 + (\omega - \omega_{ge})^2. \tag{17}$$

At resonance where $\omega = \omega_{ge}$, the probability of being in the excited state becomes

$$|c_e(t)|^2 = sin^2(\frac{\Omega t}{2}). \tag{18}$$

The Eq.18 tells a lot of information about the two-level atom model. First of all, the probability oscillates between 0 and 1 with a period of $2\pi/\Omega$, and with a larger Ω, it takes shorter time for the atom to be excited or de-excited, *i.e.* from $|c_e(t)|^2 = 0$ to $|c_e(t)|^2 = 1$ and *vice versa*. The Ω is therefore introduced as an important parameter to describe the strength of the interaction between an atom and a resonant light as *Rabi frequency*. Nevertheless, it can also be noticed that state-flipping pulse will be satisfied whenever $\Omega t = \pi$. Such a pulse will be referred to as a π *pulse* and the quantity $\theta = \int \Omega(t)dt$ is known as the *pulse area*.

3.2 Light propagation in a dispersive medium

When light propagates through a dispersive medium, the two properties that are of interest for this project are the *absorption coeffient*, α, and the *group velocity*, v_g. The frequency filter is built by creating a spectral profile with frequency-dependent $\alpha(\omega)$, while the change of v_g during the propagating, the so-called *slow light effect*, is the key point to shift the frequency of the light pulse. These two parameters, as well as how the energy of the light is stored when propagating in the medium which is important for the FSF as discussed in Sec.5, are all closely related to the dielectric constant ϵ, from which will start the discussion.

3.2.1 The dielectric constant $\widetilde{\epsilon}(\omega)/\epsilon_0$ in the harmonic oscillator model

Using the harmonic oscillator model, the frequency-dependent dielectric constant $\widetilde{\epsilon}(\omega)/\epsilon_0$ is given by

$$\frac{\widetilde{\epsilon}(\omega)}{\epsilon_0} = 1 + \frac{\Omega_p^2}{\omega_{eg}^2 - \omega^2 - i\omega\gamma_{eg}}, \tag{19}$$

where ϵ_0 is the electric permittivity of free space, ω_{eg} is the resonant frequency of the studied transition, $\gamma_{eg} = 1/T_2$ is the damping constant which equals the decay rate of the studied transition and Ω_p is the *plasma frequency* [13, 14]. The *plasma frequency*, Ω_p is given by

$$\Omega_p^2 = \frac{Ne^2}{\epsilon_0 m} f_{eg}, \tag{20}$$

where e is the electron charge, N is the concentration of active atoms, m is the mass of a free electron and f_{eg} is the oscillator strength of the studied transition varying from zero (forbidden transition) to unity.

As shown in Fig.5, the real part of the dielectric constant Re $\widetilde{\epsilon}(\omega)/\epsilon_0$ increases with ω except for the very vicinity of the resonance, where the imaginary part Im $\widetilde{\epsilon}(\omega)/\epsilon_0$ is appreciable. The term, *normal dispersion*, refers to the situation where Re $\widetilde{\epsilon}(\omega)/\epsilon_0$ increases with ω, while *anomalous dispersion* refers the reverse case. Physically, a positive imaginary part of $\widetilde{\epsilon}(\omega)/\epsilon_0$ indicates dissipation of energy from the light radiation to the medium [14], and vice versa for negative Im $\widetilde{\epsilon}(\omega)/\epsilon_0$, *e.g.* in a laser [15]. The regions where Im $\widetilde{\epsilon}(\omega)/\epsilon_0$ is positive and appreciable are called regions of *resonant absorption*. When light is propagating in these regions, the energy will be transferred and mostly stored in the medium, *e.g.* the excited ions.

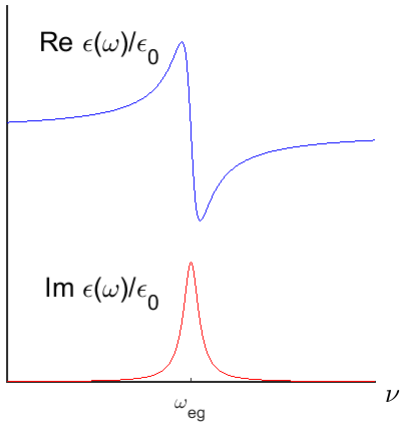

Figure 5: The frequency dependence of the real and imaginary parts of the dielectric constant $\widetilde{\epsilon}(\omega)/\epsilon_0$ in the neighbourhood of a resonance.

The real and imaginary parts of the dielectric constant $\widetilde{\epsilon}(\omega)/\epsilon_0$ satisfy the *Kramer − Kronig relations* [16]

$$\text{Re } \widetilde{\epsilon}(\omega)/\epsilon_0 = 1 + \frac{1}{\pi} P \int_{-\infty}^{\infty} \frac{\text{Im } \widetilde{\epsilon}(\omega')/\epsilon_0}{\omega' - \omega} d\omega' \tag{21}$$

$$\text{Im } \widetilde{\epsilon}(\omega)/\epsilon_0 = -\frac{1}{\pi} P \int_{-\infty}^{\infty} \frac{\text{Re } \widetilde{\epsilon}(\omega')/\epsilon_0 - 1}{\omega' - \omega} d\omega', \tag{22}$$

where P refers to the *Cauchy* principal value of the integral.

3.2.2 The absorption coefficient and refractive index

When propagating in the medium, the intensity of the light wave decreases as $e^{-\alpha l}$ with l the distance it has travelled. The absorption coefficient α can be written in the term of the wave number k as

$$k = \beta + i\frac{\alpha}{2}, \tag{23}$$

which is related to the dielectric constant by the *dispersion relation*:

$$k = \sqrt{\mu\epsilon}\ \omega = n\frac{\omega}{c}. \tag{24}$$

The last relation in Eq.24 introduces the *index of refraction*, n, defined as

$$n = \sqrt{\frac{\mu}{\mu_0}\frac{\epsilon}{\epsilon_0}}. \tag{25}$$

Taking the relative permeability $\mu/\mu_0 = 1$, the $\alpha(\omega)$ and $n(\omega)$ could be approximated as

$$\alpha(\omega) = \frac{2\omega}{c}\mathrm{Im}(\sqrt{\frac{\widetilde{\epsilon}(\omega)}{\epsilon_0}}) \tag{26}$$

and

$$n(\omega) = \mathrm{Re}(\sqrt{\frac{\widetilde{\epsilon}(\omega)}{\epsilon_0}}). \tag{27}$$

Linked by the *Kramer-Kronig relations* given in Eq.21 and Eq.22, the refractive index can be calculated using the absorption coefficient obtained from the spectrum. The frequency dependence of the $\alpha(\omega)$ and $n(\omega)$ in the neighbourhood of a resonance is shown in Fig.6.

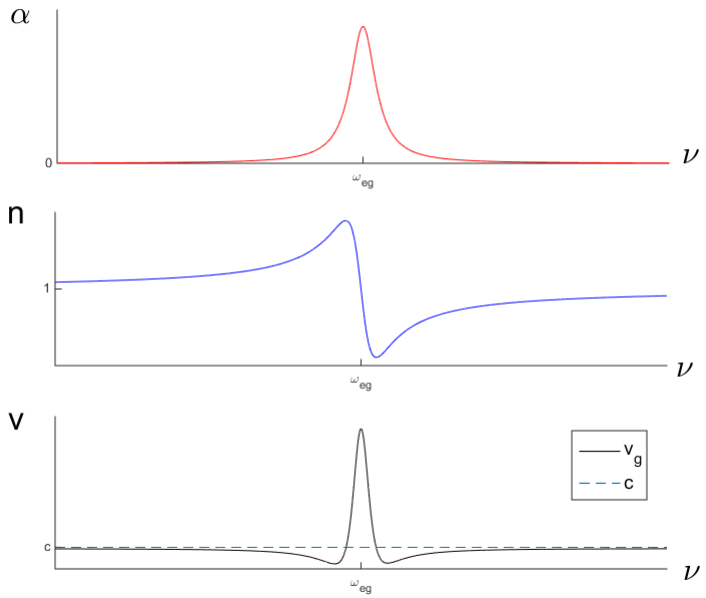

Figure 6: The frequency dependence of the $\alpha(\omega)$, $n(\omega)$ and $v_g(\omega)$ in the neighbourhood of a resonance. The group velocity is compared with the group velocity in non-dispersive medium $c = c_0/n(\omega)$.

3.2.3 The group velocity v_g

For a light pulse propagating in a dispersive medium, the *group velocity* is defined as

$$v_g = \frac{\partial\omega(k)}{\partial k}, \tag{28}$$

with which the pulse travels undistorted in shape. It is usually more convenient to deal with v_g as a function of ω instead of k in the form of

$$v_g(\omega) = \frac{1}{\partial k(\omega)/\partial\omega} = \frac{c_0}{n(\omega) + \omega\frac{\partial n(\omega)}{\partial\omega}}. \tag{29}$$

The frequency dependence of the $v_g(\omega)$ in the neighbourhood of a resonance is given in Fig.6.

3.3 The slow light effect

From Fig.6, it can be seen that there are two regions where $v_g < c$, the slow light region, and one region where $v_g > c$, the fast light region. The *slow light effect* is defined as a decrease in the group velocity in the slow light region. However, if the pulse is in the resonant absorption region of a strong absorption line, it will be absorbed and therefore distorted so that the slow light effect can not be observed. In 1970, Garret and McCumber [17] theoretically proved that, if the absorbers are not too thick and the width of absorption line is much smaller than that of the pulse, a Gaussian pulse will more or less retain its shape with the peak moving at the group velocity defined in Eq.29. If the absorber has a narrow absorption line, the slow light effect will also occur when the pulse centres outside the resonant absorption region due to the off-resonant interaction between the light and the absorber [18]. The slow light effect observed in this project is such off-resonant slow light.

Before further discussion, we first introduce the factor $S(\omega)$ describing the reduction of the group velocity as

$$S(\omega) = \frac{c}{v_g} = n(\omega) + \omega\frac{\partial n(\omega)}{\partial \omega}. \tag{30}$$

For the frequencies far from the FWHM of the absorption, $|\omega - \omega_{eg}| \gg \gamma_{eg} = 1/T_2$, where the slow light effect is caused by the off-resonant interaction between the light and the medium, $S(\omega)$ can be approximated as [13]

$$S(\omega) \approx 1 + \frac{L_c}{L_\alpha}, \tag{31}$$

with $L_c = \frac{c}{\gamma_{eg}} = c \cdot T_2$ the length over which the light preserves its phase and $L_\alpha = 1/\alpha$ the length over which the light preserves its intensity [13]. Eq.31 indicates that for an absorption with long coherence time T_2, *i.e.* long L_c, the slow light effect will be conspicuous. This is consistent with requirement of narrow absorption line, Γ_h, for the slow light effect discussed in last paragraph, given that $T_2 = 1/\pi\Gamma_h$ as defined in Eq.4.

Since shifting the frequency of the light pulse equals altering the energy of it, it is important to understand how the energy is distributed or stored when light is propagating in the crystal. Using the classical model for the electromagnetic field, the energy density of the light pulse in vacuum is given as

$$W_{vac} = \frac{1}{16\pi}(\epsilon_0|E|^2 + \mu_0|H|^2), \tag{32}$$

with E and H the amplitudes of the electric and magnetic components of the field. A light pulse propagating in a slow light region will be compressed. As a result, the energy density will be increased. However, since the amplitudes of the pulse, *i.e.* E and H, remain the same, the extra energy density can only be stored in the medium. In analogy with how the energy is stored when light propagating in the resonant absorption region discussed in Sec.3.2.1, the energy density here can be understood as being stored in the form of atomic polarization. Instead of exciting the atom and transfering the energy to the atom until its decay, the energy in this case can be viewed as being stored in the coupling between the electromagnetic field of the light wave and the atomic polarization as shown

in Fig.7. It can be understood as a coherent transfer of the energy between the light pulse and the medium. The longer the time the energy is preserved in the polarization, the slower the light propagates.

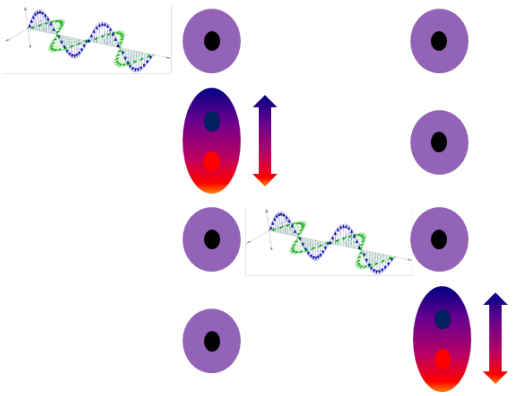

Figure 7: The off-resonant slow light can be interpretated as a coupling between the electromagnetic field of the light wave and the atomic plorization of the absorber. The longer the time the energy is preserved in the polarization, the slower the light propagates.

Denoting the energy density stored in the medium as W_{med}, the group velocity v_g can be given as a function of W_{vac} and W_{med} as [19, 20]

$$v_g = \frac{c/n}{1 + W_{med}/W_{vac}}. \tag{33}$$

It is clearly shown here that the more the energy preserved in the polarization, *i.e.* larger W_{med}, the slower the light is propagating, *i.e.* smaller v_g.

4 Spectral hole-burning technique

The spectral hole-burning technique is used in this project to create the spectral filter. The method and the detailed spectral structure will be discussed in this section.

4.1 Persistent spectral hole-burning by optical pumping

When light passes through an absorber it will be absorbed if the frequency of the light coincides with the absorption profile. The spectral hole-burning technique, illustrated in Fig.8a, refers to the experimental method where a laser is used to excite a narrow

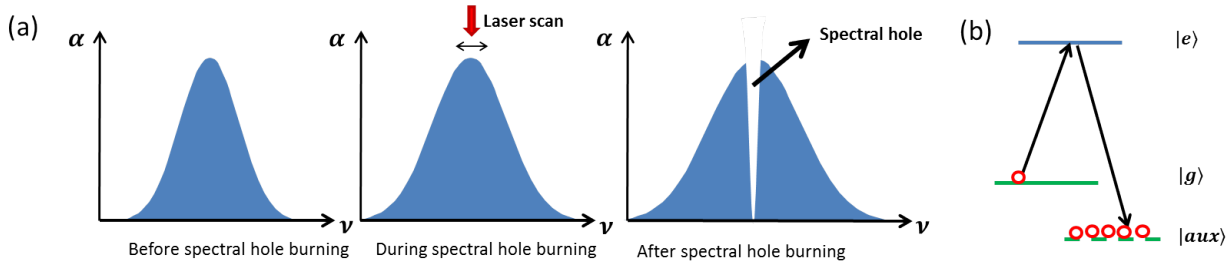

Figure 8: The spectral hole-burning technique. (a) A laser is used to create a hole in an inhomogeneous absorption line profile, so that the light with the frequency within the hole will no longer be absorbed. (a) The absorber is excited and then decaying to other hyperfine levels of the ground state, the auxiliary states.

portion of an inhomogeneous absorption line profile, so that the light with the frequency within that narrow portion can no longer be absorbed. The narrow portion is referred to as the transparent *hole* and it will remain until the absorbers return to their original ground states. If the absorbers are transferred to other states with lifetime considerably longer than that of the excited state, the hole will be addressed as *persistent*. Such persistent hole burning can be achieved by many mechanisms, *e.g.* photoionization [21] and photochemical reactions [22]. The mechanism used in this project, as shown in Fig.8b, is due to absorbers being excited and then decay to other long-lived hyperfine levels of the ground state of the absorber (the three hyperfine levels of ${}^3H_4(1)$ of $Pr^{3+} : Y_2SiO_5$ have a lifetime of a few minutes [23]). The absorber (ion) will therefore be trapped in other states and the narrow homogeneous linewidth of the transition makes it possible for the laser to only interact with a narrow portion of all the absorbing ions.

4.2 Side-holes and anti-holes

This spectral hole-burning technique can be modelled by the population distribution of the hyperfine sublevels in the ground state (population distribution model). For the frequencies with depleted population because the corresponding ions have been transferred to other hyperfine levels, a hole with decreased absorption is created. Similarly, for the frequencies with increased population, *anti-holes* with increased absorption are created. *Side-holes* will occur if there are more than one sublevel in the excited state at the frequencies equal to the corresponding transitions. Fig.9 shows the main hole, side-holes and anti-holes created by a narrow laser burning at the $|g_2\rangle \leftrightarrow |e_2\rangle$ transition of the ${}^3H_4(1) \leftrightarrow {}^1D_2(1)$ of Pr^{3+} with three sublevels in both excited and ground state.

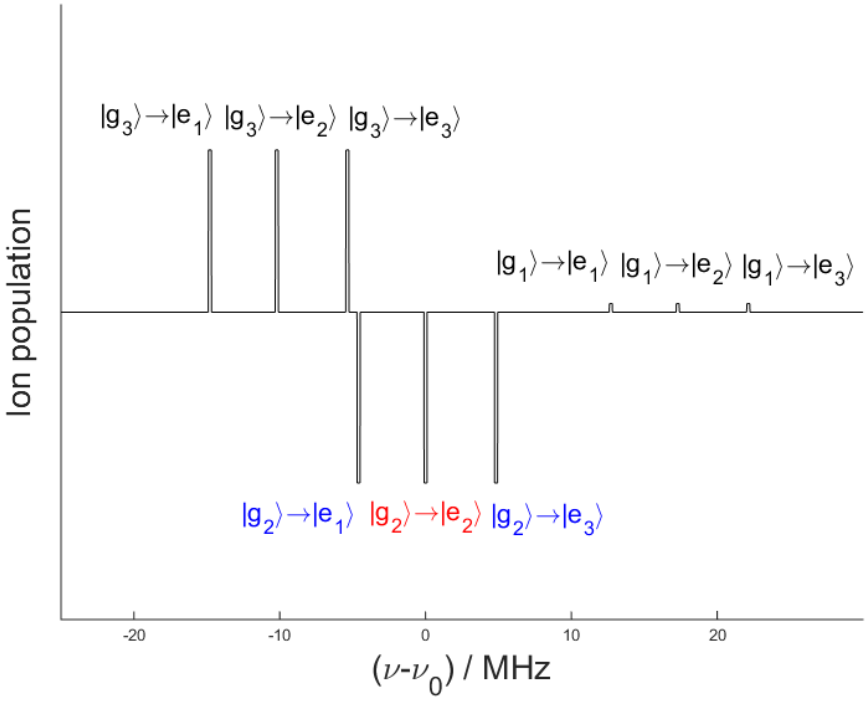

Figure 9: The main hole (red), side-holes (blue) and anti-holes (black) and the corresponding transitions of a single group of ions being burning by a narrow laser centred at ν_0, the $|g_2\rangle \leftrightarrow |e_2\rangle$ transition.

Table 3: The relative oscillator strengths of the nine transitions of ${}^3H_4(1) \leftrightarrow {}^1D_2(1)$ of $Pr^{3+} : Y_2SiO_5$.

	e_1	e_2	e_3
g_3	0.56	0.38	0.06
g_2	0.39	0.60	0.01
g_1	0.05	0.02	0.93

The different amplitudes of the two groups of anti-holes are due to the different oscillator strengths of different transitions listed in Table 3. For instance, for the ions being excited to $|e_2\rangle$, their probability to decay to $|g_3\rangle$ (0.38) is much larger than to $|g_1\rangle$ (0.02), so the amplitudes of the anti-holes that correspond to the transitions from $|g_3\rangle$ is much higher than those from $|g_1\rangle$.

However, the real hole-burning spectrum is more complicated. Because of the inhomogeneous broadening, the transition frequencies of different ions will differ from each other. Since the hyperfine splitting is much smaller compared with the inhomogeneous broadening, the burning frequency of the laser, ω_{burn}, will be resonant with different transitions for different groups of ions as shown in Fig.10.

As a result, the side-holes and anti-holes of different ions occur at different frequencies of the inhomogeneous broadening profile. Since there are nine groups of ions with different transitions resonant with the laser field, and each group has two side-holes and six anti-holes, as shown in Fig.9, there should be $2 \times 9 = 18$ side-holes and $6 \times 9 = 54$ anti-holes in total. However, some of the side-holes and anti-holes from different groups of ions will overlap. As a result, only 6 side-holes and 42 anti-holes will occur as shown in Fig.11.

Using a chirped laser pulse scanning within the inhomogeneous profile, a pit (a wide hole) can be created. It can be shown that because the ions have to be in one of the three

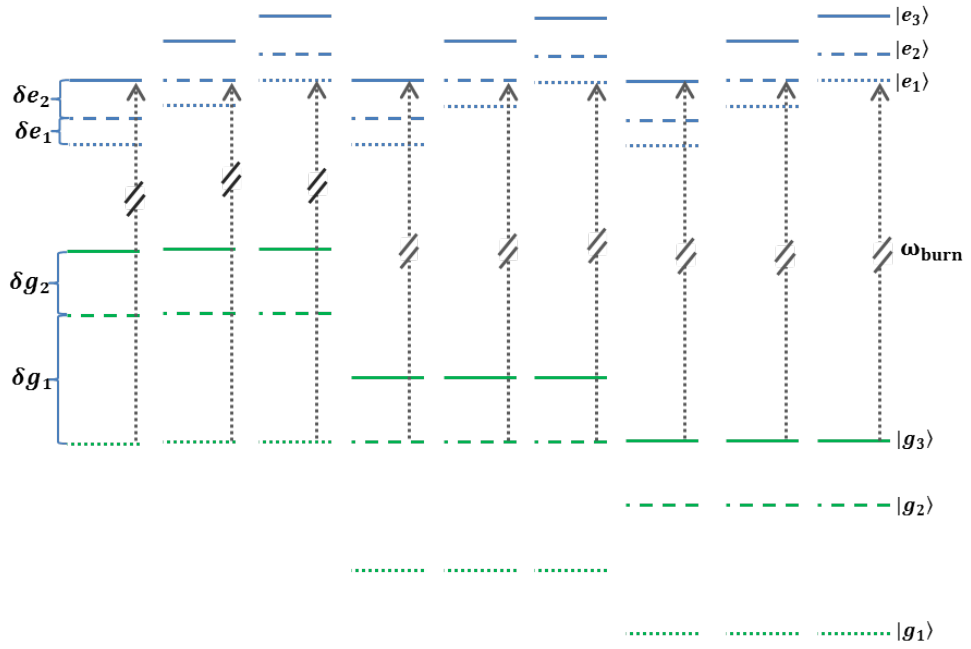

Figure 10: Sketch for the energy levels for different groups of ions. The frequency of the laser will be resonant with different transitions for different ions because of the inhomogeneous broadening. For the ${}^3H_4(1) \leftrightarrow {}^1D_2(1)$ of $Pr^{3+} : Y_2SiO_5$, there are nine different groups.

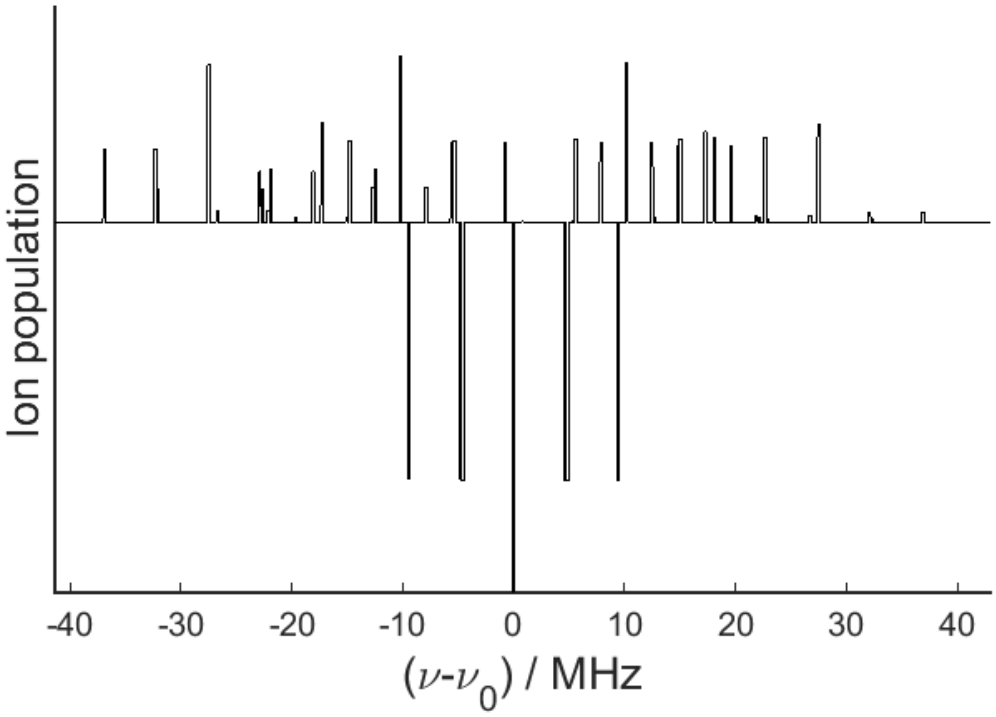

Figure 11: The spectrum for burning with a narrow laser centered at ν_0. The resonant transition of the corresponding ion group and the transition of the absorption of each hole are listed in the Table 4.

Table 4: The resonant transition of the corresponding ion group and the transition of the absorption of the holes in Fig.11, with red for the main hole, blue for the side holes and black for the anti-holes.

	Resonant Transitions of the group of ions								
	$\|g_1\rangle \leftrightarrow \|e_1\rangle$	$\|g_1\rangle \leftrightarrow \|e_2\rangle$	$\|g_1\rangle \leftrightarrow \|e_3\rangle$	$\|g_2\rangle \leftrightarrow \|e_1\rangle$	$\|g_2\rangle \leftrightarrow \|e_2\rangle$	$\|g_2\rangle \leftrightarrow \|e_3\rangle$	$\|g_3\rangle \leftrightarrow \|e_1\rangle$	$\|g_3\rangle \leftrightarrow \|e_2\rangle$	$\|g_3\rangle \leftrightarrow \|e_3\rangle$
$\|g_1\rangle \leftrightarrow \|e_3\rangle$	-9.4	-4.8	0	-26.7	-22.1	-17.3	-36.9	-32.3	-27.5
$\|g_1\rangle \leftrightarrow \|e_2\rangle$	-4.6	0	4.8	-21.9	–17.3	-12.5	-21.1	-27.5	-22.7
$\|g_1\rangle \leftrightarrow \|e_1\rangle$	0	4.6	9.4	-17.3	–12.7	-7.9	-27.5	-22.9	-18.1
$\|g_2\rangle \leftrightarrow \|e_3\rangle$	7.9	12.5	17.3	-9.4	-4.8	0	-19.6	-15.0	-10.2
$\|g_2\rangle \leftrightarrow \|e_2\rangle$	12.7	17.3	22.1	-4.6	0	4.8	-14.8	-10.2	-5.4
$\|g_2\rangle \leftrightarrow \|e_1\rangle$	17.3	21.9	26.7	0	4.6	9.4	-10.2	-5.6	-0.8
$\|g_3\rangle \leftrightarrow \|e_3\rangle$	18.1	22.7	27.5	0.8	5.4	10.2	-9.4	-4.8	0
$\|g_3\rangle \leftrightarrow \|e_2\rangle$	22.9	27.5	32.3	5.6	10.2	15.0	-4.6	0	4.8
$\|g_3\rangle \leftrightarrow \|e_1\rangle$	27.5	32.1	36.9	10.2	14.8	19.6	0	4.6	9.4

hyperfine levels of the ground state after relaxation from the excited state, the width of the pit is limited by

$$\delta_{max} = (\delta g_1 + \delta g_2) - (\delta e_1 + \delta e_2) = 18.1 \text{ MHz}, \tag{34}$$

with which all the ions that have been moved out of the pit have an auxiliary hyperfine sublevel to decay to.

5 The frequency shift filter

In this section, the absorption structure of the FSF will be discussed in Sec.5.1. With such a spectral structure, the FSF will be able to (1) have tunable passband, (2) delay the pulse that propagates in the passband, (3) shift the frequency of this pulse, and (4) have 2π acceptance angle for the light. The creation and the simulation for the structure will be discussed in Sec.5.2 and Sec.5.3.

5.1 The spectral structure

The spectral structure of the FSF is shown in Fig.12. A $1 \sim 2$ MHz hole is burnt with no absorption, so that it works as a filter with a $1 \sim 2$ MHz passband. Furthermore, since the homogeneous linewidth of the Pr ion (about 1 kHz at temperature below 5 **K**) is much smaller than the spectral FWHM of the target signal to be shifted, *e.g.* the UOT signal which is at the order of a MHz, a Gaussian pulse centred at the hole will experience the slow light effect due to the off-resonant interaction between the light field and the ions outside the hole as discussed in Sec.3.3. The slow light effect will slow down the signal and thus separate it from the background noise that has not been completely absorbed by the filter. With this structure, the signal will be slowed down to $c/10^4 \sim c/10^5$, which means that more than 99.99% of the energy density is stored in the medium when light is propagating in the filter according to Eq.33. Therefore, by changing the resonace frequency of the medium by external means, the energy will be altered and so will the frequency of the signal after passing through the medium.

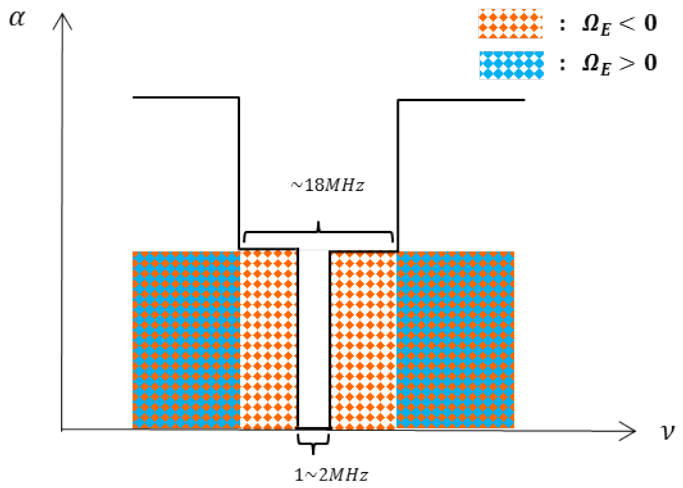

Figure 12: The spectral structure of the FSF. The red and blue dots refer to the two groups of ions with opposite directions of their Stark shifts. A narrow hole of $1 \sim 2$ MHz is burnt in a frequency region where the surrounding ions all have the same Stark shift. This causes the off-resonant interaction between the light field and the medium to only take place for ions with the same Stark shift.

The energy stored in the medium is manipulated by applying a static electric field on the crystal. As discussed in Sec.2.3.2, when applying a direct current electric field $\boldsymbol{E}$, the ${}^3H_4(1) \leftrightarrow {}^1D_2(1)$ transition will experience a linear Stark shift, $\Omega_E = \delta\boldsymbol{\mu} \cdot \boldsymbol{E}/\hbar$, with the dipole moment $\delta\boldsymbol{\mu}$ either parallel or anti-parallel with the **E** field as shown in Fig.2.3.2. In order to shift the frequency of the light pulse efficiently, it is important to separate these two groups of ions so that the off-resonant interaction between the light field and

the medium only take place for ions with the same Stark shift. As it is shown in Fig.12, the hole is only surrounded by one group of ions with identical Stark shift.

5.2 Creation of the spectral structure

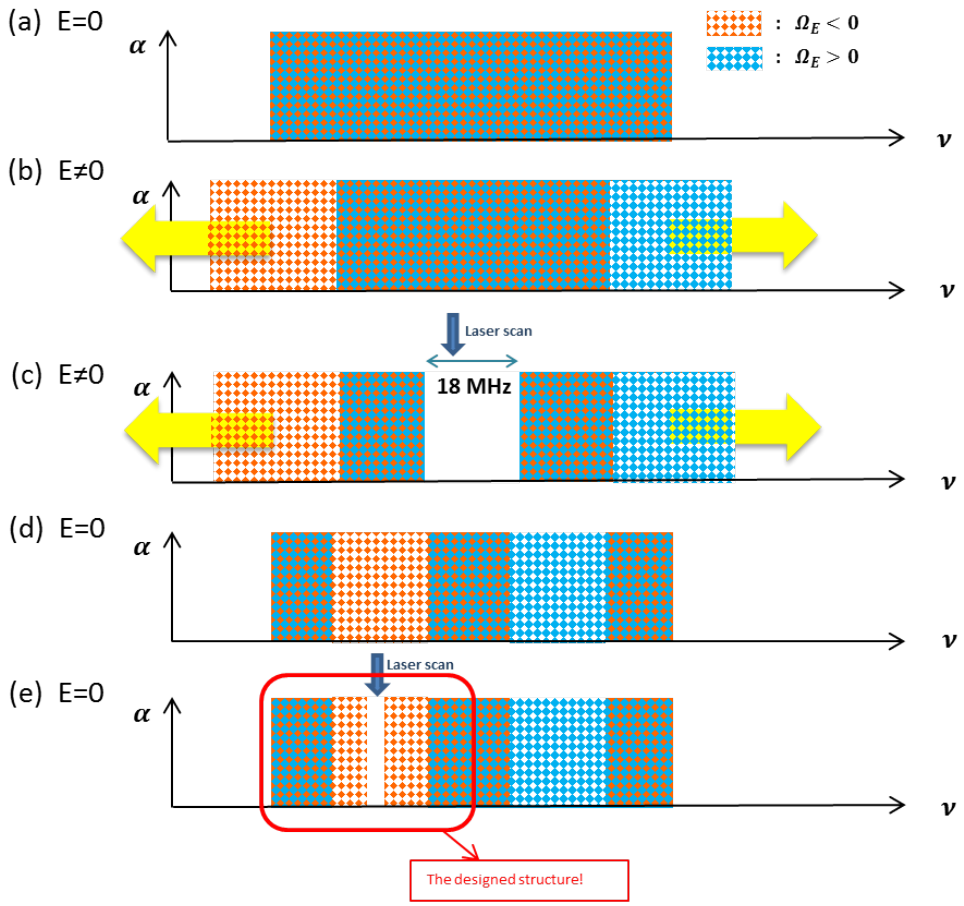

Figure 13: The FSF is created within 100 MHz in the center of the inhomogeneous profile which has the linewidth of a few GHz. The absorption coefficient is thus treated as being the same in the region used for the creation. For simplicity, only the isolate absorption profile of interest is shown. (a) Before structure creation, the absorption profiles of the two groups of ions are the same. (b) When applying an electric field, the absorption profile of the two groups of ions will shift to higher and lower frequency respectively. Since the inhomogeneous linewidth is much larger than the frequency shift, the absorption profile looks no difference in the region of interest. (c) An 18 MHz pit is created using spectral hole burning with the electric field on. (d) By turning off the field, the absorption profiles of the two groups of ions will shift back to their original positions. As a result, the pit will split into two parts with each one filling with only one kind of ions. (e) The structure is completed by creating a hole centred at the pit of one kind of ions.

The process of the structure creation is illustrated in Fig.13, where only the isolate absorption profile within the frequency region used for the creation (less than 100 MHz) is used for simplicity. The FSF is created at the center of the inhomogeneous profile. Since the inhomogeneous profile which has the linewidth of a few GHz is much wider than the frequency range used for the creation, the absorption coefficient could be treated as being the same all across the frequency region used for the structure creation as shown in 13a. The creation method proposed in this project is done with a chirped laser and a

controllable electric field. When an electric field is applied, the absorption profile of the two groups of ions will be shifted to the higher and lower frequency respectively as shown in Fig.13b. The structure can be created in two steps: first an 18 MHz pit is created with the electric field turned on (as in Fig.13c). When turning off the field, the pit will be split into two parts with each one filling with only one kind of ions as shown in Fig.13d. The structure will then be completed by creating a $1 \sim 2$ MHz hole centred at the pit of only one kind of ions (as in Fig.13e). The frequency difference between the pit creation laser and the hole creation laser can be calculated by the dipole moment according to Eq.5.

5.3 The simulation

In this section, the simulation of the spectral profile of the FSF will be presented. Since the electric filed is used during the creation of the spectral structure, it will be used as an input to the simulation of the spectral profile. The electric field applied on the crystal is thus simulated as well.

5.3.1 The simulation of the electric field

Crystal coating In order to apply an electric field on the crystal, the crystal is coated with a 2000 Å Au layer which acts as the electrical conductor to the crystal. As shown in Fig.14, the coating is separated into two parts. This is due to the fact that the crystal will also be used in another experiment that wishes to apply different electric fields in the two parts of the crystal. Since the Au coating is not able to attach to the crystal firmly, a 50 Å Ti layer is precoated as the glue between the crystal and the Au coating. The crystal was coated at *NanoLund*. The contract and the *Solidwork* drawings of the mask used for the coating is attached in Appendix A.

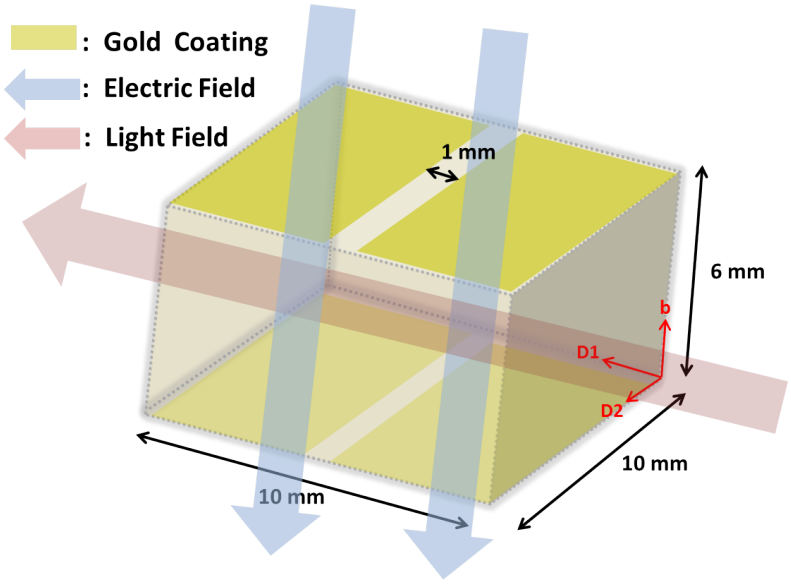

Figure 14: The $Pr^{3+} : Y_2SiO_5$ crystal is sized by 10 mm × 10 mm × 6 mm. Two surfaces are coated with 2000 Å Au so that the electric field could be applied along the b axis. The light is propagating along the D1 axis so that it will be polarized along the D2 axis for higher absorption.

The electric field The gap between the two electrodes makes the electric field no longer homogeneous along the path of the light propagation in the crystal. This inhomogenity

may affect the performance of the FSF since the electric field is used during the creation and the shift of the frequency of the passband and the light pulse. The electric field is thus modeled using *Comsol*. By setting the electric potential at both the anticathode and cathode, the *Comsol* will give the electric potential inside the crystal by calculating the *Maxwell's equations*. The 3D result is shown in Fig.15a. The light propagates along the D1 axis and is focused down to $\phi \sim 100$ μm inside the crystal. In this region, the inhomogeneity of the electric field along b axis and D2 axis is less than 0.3 % with the electric field less than 200 V/cm, the maxium field that could be used in the experiment. As the effect of this inhomogeneity is small, they are ignored in the spectral hole burning simulations. The inhomogeneity of the relative electric field E/E_{max} along D1 in the center of the crystal is shown in Fig.15b with the average electric field in the crystal $E_{aver} = 0.992E_{max}$. The inhomogenity is small in the center and the maxium difference of the field is 2.3 %.

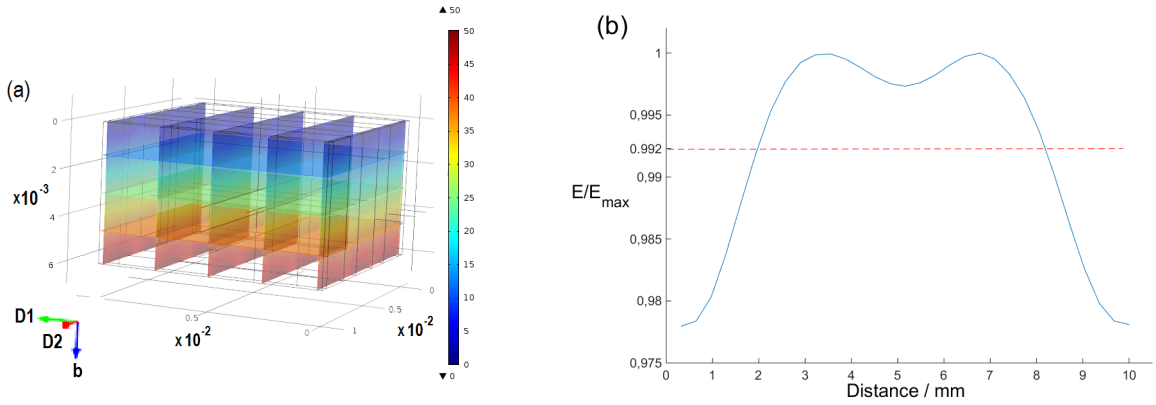

Figure 15: The simulation of the electric field in the crystal using *Comsol* with applied voltage $V = 50$ V. (a) The 3D results. The amplitude of the electric potential is presented with different color as shown in the colors bar. (b) The line result of E/E_{max} along D1 axis centered at the $D2$-b surface. The red dash is the average of the field in the crystal with $E_{aver} = 0.992E_{max}$.

5.3.2 The simulation of the FSF

The *Matlab* code used for the simulation is based on the hole burning simulation created by former Ph.D. student Mattias Nilsson using the population distribution model discussed in Sec.4.2. The code is modified by the author so that the electric field can be applied during the pit/hole creation. Instead of ion population, the relative absorption coefficients are calculated. The structure is created as discussed in Sec.5.2 with the applied electric field $E = 147$ V/cm (same as in the experiment with applied voltage $V = 88$ V). The simulation results are given in Fig.16a. The inhomogeneous electric field calculated by *Comsol* with $V = 88$ V is implemented in the simulation as shown in Fig.16b. This is done by applying different electric fields on different sets of the ions according to the field given in Fig.15b, and the result given here is the average of the whole sets. Compared with Fig.16a and Fig.16b, little difference can be noticed. The edge of the pit/hole is slightly more smooth with the inhomogeneous electric field, which means that a bit more absorption is introduced at the edge of the pit/hole as some of the ions are more/less moved because of the inhomegeneity of the electric field.

With the $Kramer - Kronig$ relations given in Eq.21 and Eq.22, the refractive index of the hole can be calculated from the absorption coefficients. The frequency dependence

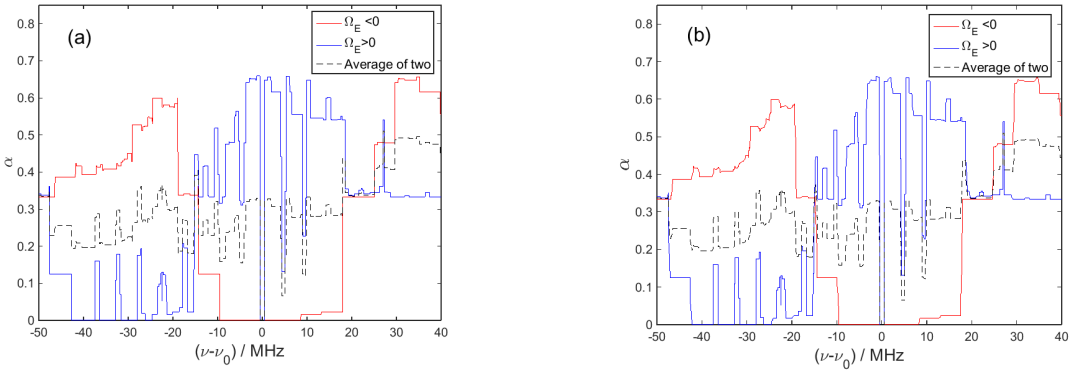

Figure 16: The *Matlab* simulation of the FSF structure. The red(blue) solid line represents the ions with dipole moments parallel(antiparallel) with the electric field and the black dots is the average of the two. The simulation gives the relative absorption coefficients, which is 0.33 before hole burning. (a) The frequency-absorption for the structure. (b) The frequency-absorption for the structure with inhomogeneous E field calculated by *Comsol*.

of the refractive index is plotted in Fig.17. As given in Eq.30, the slow light factor $S(\omega) = c/v_g$ increases with $\partial n(\omega)/\partial\omega$. So the light with the frequency inside the hole, where $n(\omega)$ varies rapidly with ω, will experience conspicuous slow light effect. As a higher on-off ration of the absorption, which is defined as the ratio of the absorption inside vesus the absorption outside the hole, leads to a larger $\partial n(\omega)/\partial\omega$, the slow light effect in the main hole will be stronger than it in the two side holes where the on-off ratio of the absorption is smaller.

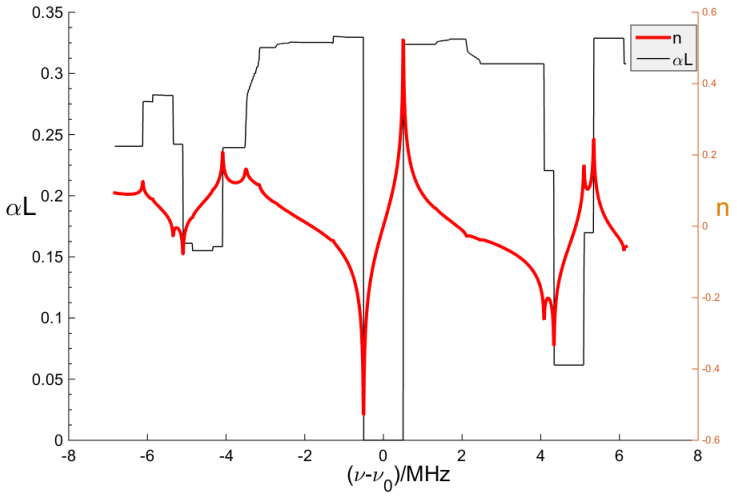

Figure 17: The frequency dependence of the refractive index (red) calculated from the absorption coefficients (black). The $\partial n(\omega)/\partial\omega$ is larger in the main hole than it is in the side-holes. As larger $\partial n(\omega)/\partial\omega$ leads to a larger slow light factor $S(\omega)$ and hence a strong slow light effect, the slow light effect is most conspicuous in the main hole.

6 Experiment

The experiment is conducted in the lab of the *Quantum Information* group. The experimental setup, pulse sequence and the applied electric field are discussed in Sec.6.1-6.2, while the results discussions are discussed in Sec.6.3.

6.1 Experimental setup

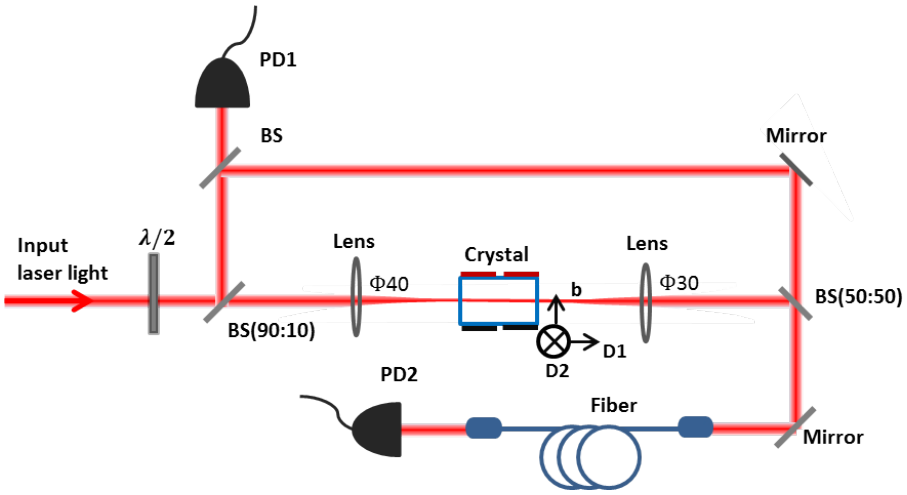

Figure 18: The experimental setup. The laser path is represented by the red line. After passing through the $\lambda/2$ plate, it is split by a 90:10 beam splitter (BS), where the stronger one is focused onto the crystal and the weaker one is used as a reference beam. The reference beam will be further split into two parts. One part is detected by PD1, and the other part is used as a local oscillator to beat with the transmitted beam after passing through the crystal. Both the main beam and the local oscillator beam are coupled into a single mode fibre and then focused on the detector PD2. The optical components are given with their names.

The experimental setup is shown in Fig.18. The laser centred at 606 nm is generated by a coherent $699-21$ dye laser pumped by a 6 Watt $Nd:YVO_4$ $Verdi-V6$ laser at 532 nm. The laser is frequency stabilized against an external cavity and accurate control of the phase and amplitude of the pulses is provided through an Acusto-Optic Modulator. After passing through a λ-half plate, which is used to turn the polarization of the incoming beam to the $D2$ axis of the crystal, the light is split by a 90:10 beam splitter (BS). The stronger beam is focused onto the crystal, while the weaker one is used as the reference beam. The reference beam is further split by another BS, where one is sent into the detector PD1 while another one is used as a local oscillator to beat with the transmitted beam after the crystal. Both the main beam and the local oscillator beam are coupled into a single mode fibre and then focused onto the detector PD2. The frequency of the transmitted beam can then be calculate from the beating pattern with the local oscillator. The local oscillator is only used when investigating the transmitted beam frequency. The reference beam detected by PD1 can be used to calibrate the intensity fluctuation of the laser or calculate the slow light effect of the FSF by comparison with the transmitted beam. The two detectors used here are the photo detectors $PDB450A$ provided by Thorlabs.

The crystal is fixed in a crystal holder designed by former project students Akash Yadav and Lalit Gupta [24]. Since the crystal holder is designed for another crystal which is 10 mm high while current crystal is only 6 mm high, a 4 mm copper piece is made to adapt this crystal to the holder. The whole set is then put into a cryostat and the crystal

is then cooled down to about 2.1 **K** by liquid helium. Since electric fields will be applied, it is important to check the breakdown voltage. It is safe for this project: the breakdown voltage for liquid helium is more than 10 kV/mm [25], while electric fields used in this project is less than 20 V/mm.

6.2 The pulse sequence and electric field

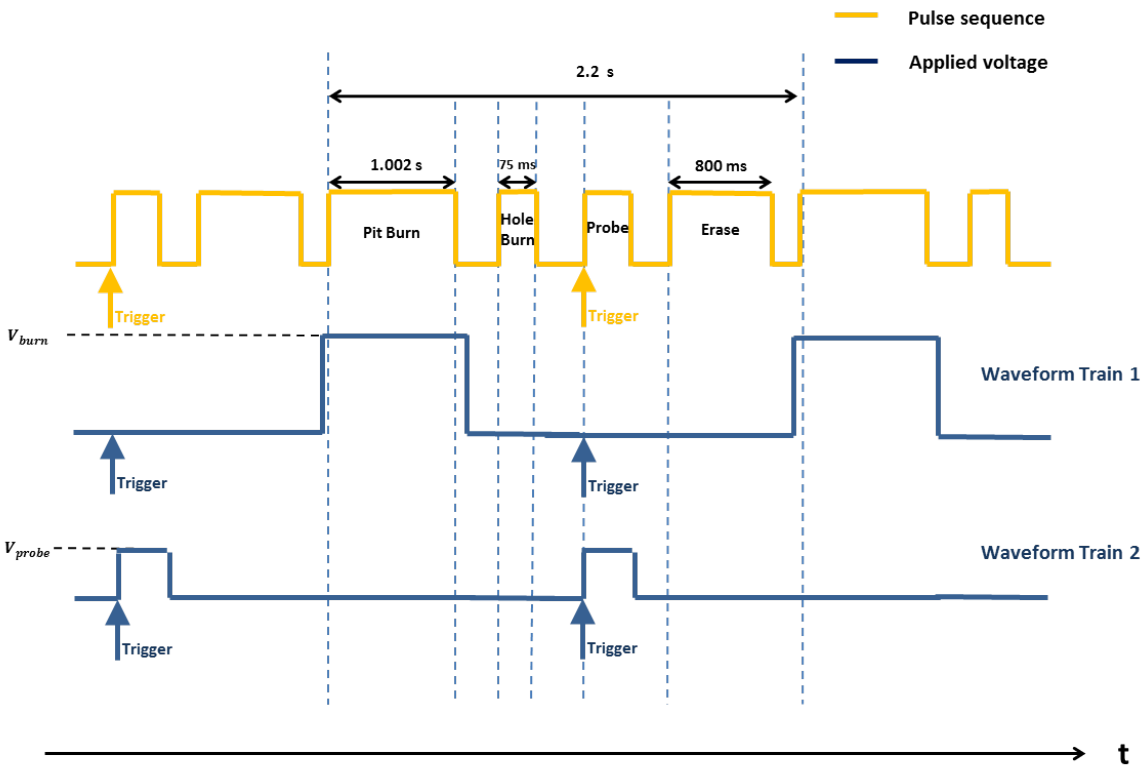

Figure 19: The pulse sequence shown as the yellow trace and electric field shown as the blue line of the experiment. The laser pulse sequence includes the 18 MHz pit burning sequence (1.002 s), the narrow hole burning sequence (75.4 ms), the probe sequence and the erase sequence (800 ms). The external voltages applied are shown as the blue traces. Two waveforms are generated for the 18 MHz pit creation and the probe with the trigger synchronous as the probe.

The pulse sequence is shown in Fig.19. The whole sequence starts with the structure burning pulses to create an 18 MHz pit and follows by a 1 $\sim$ 2 MHz hole burning pulses. π *pulse* is used for burning to excite the ions more efficiently. The burning pulse sequence used for the 18 MHz pit is given in *Ref* [26]. With this pulse sequence, the ions outside the pit are further shifted away. This will help to get rid of the absorption introduced by the tails of the absorption spectrum of these ions. With them being shift away, the pit is optimized. Moreover, as it is given in Eq.30, the light will be more slowed down with larger $\partial n(\omega)/\partial\omega$, which could be achieved by a sharper edge of the hole. The optimal burning sequence for such a hole is studied by a former masters student Philip Dalsbecker of our group and the one used in this project is given in his master's thesis [27]. After the structure creation, a probe pulse will be sent in. It can either be a frequency chirped pulse for reading out the structure or a 1 μs long Gaussian pulse to test the frequency shift. Finally, erase pulses (a frequency scan pulse with 200 MHz span and maximum intensity) is sent in to erase the structure. One sequence takes about 2.2 s with the pit

burn pulse 1.002 s, the hole burn pulse 75.4 ms, the erase pulse 800 ms and the changeable probe pulse.

The electric field is used during the structure creation and to shift the frequency of the hole as well as the light pulse. It is generated by the arbitrary waveform generator *TGA1240* provided by *Thurlby Thandar Instruments* and amplified by the High-Voltage Amplifier MODEL:3211 from *New Focus*. Two waveform trains are generated: one for the pit creation; one for the probe. The precision of the wave train is limited to the larger one of either 0.002% of the pulse length or 25 ns. So in order to control the probe field more precisely, the trigger is given at the same time as the probe pulse.

6.3 Results and discussion

6.3.1 Structure readout

By sending in a chirped readout pulse that scans the frequency area of interest, the absorption spectrum will be able to be calculated from the detected transmission spectrum. Since the transmission light decreases exponentially as $I_{trans} = I_{in}e^{-\alpha L}$, the transmission light will be too weak to be distinguished from the noise when reading out the structure created in the center of the inhomogeneous profile where αL is large. Therefore, the whole structure is read out at 605.947 nm, 16 GHz away from the center of the inhomogeneous profile at 605.977 nm.

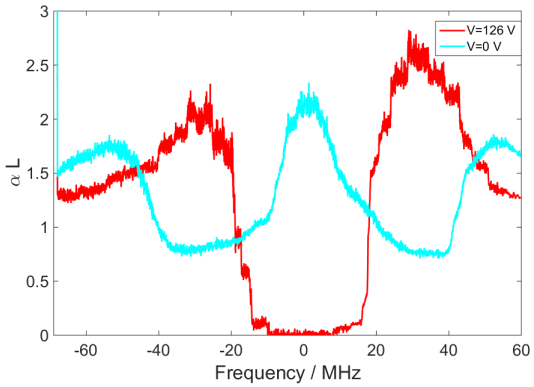

Figure 20: The $\sim$ 18 MHz pit sturcture read out before and after applying the external voltage. The 0 MHz corresponds to the center of the pit. The pit is created with 126 V voltage applied on the crystal (red line). It will be split into two 'half-pit' when the voltage is switched off (blue line).

The original pit structure is shown as the red line in Fig.20 with the 0 MHz corresponds to the center of the pit. It can be clearly seen that the pit is split into two parts (shown by blue line) when the electric field is switched off because of the different dipole moments. As discussed in Sec.5.3.2, the slow light effect will be enhanced with a larger on-off ratio of the absorption. To increase the on-off ratio, instead of the 126 V as used in Fig.20, an 88 V voltage is applied in the experiment so that the anti-holes of one kind of ions will overlap with the pit of the another kind of ions as shown in Fig.21. The hole structure of both 1 MHz and 2 MHz passband is shown in Fig.22.

6.3.2 The slow light effect

To detect the slow light effect of the FSF, a Gaussian pulse is used. Pulses with different time durations (200 ns, 300 ns, 500 ns, 1 μs) centred at the 0 MHz are sent into the FSF.

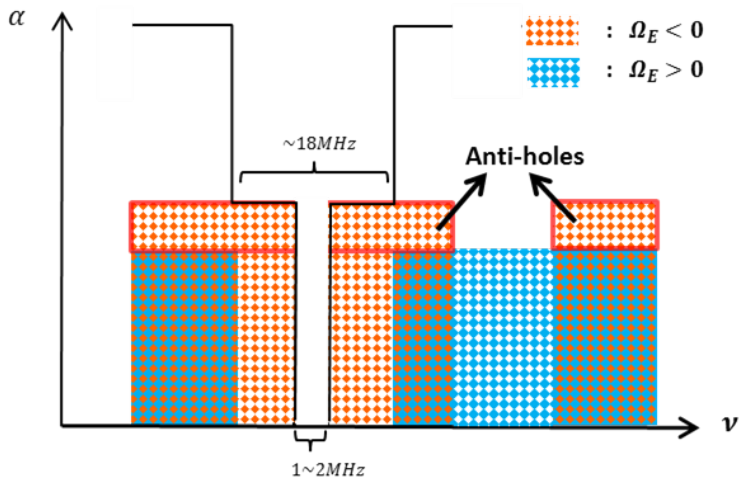

Figure 21: The optimal FSF structure. With the anti-holes of the same kind of ions overlapping the pit, a higher on-off ratio of the absorption will be achieved compared with the FSF structure in Fig.12. The anti-holes of the other kind of ions (the blue one) is not shown in the figure.

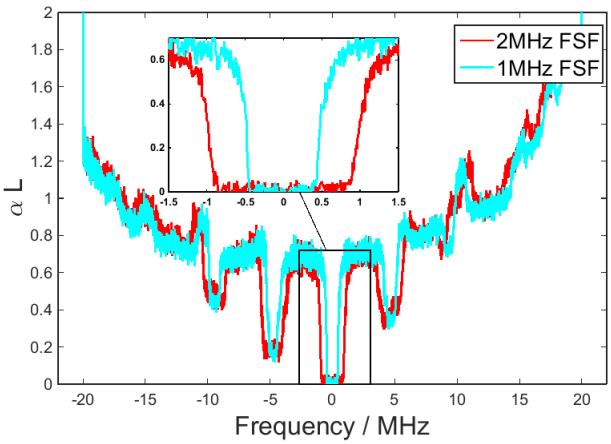

Figure 22: The hole structure read out. The main hole at 0 MHz is magnified as shown in the insert. Both 1 MHz hole (blue) and 2 MHz hole (red) are prepared as shown.

Since the light path inside the crystal is given as 10 mm, the group velocity of the pulse can be calculated by the time delay between the incoming beam and transmitted beam. As shown in Fig.23, the beam has been delayed for about 4.3 μs for the 1 MHz FSF and 2.9 μs for the 2 MHz FSF. The time delay is slightly different for pulses with different time durations. This is mainly due to the higher-order dispersion of the pulse and the spontaneous decay of the excited ions [18], which also introduce the intensity drop and the breakup in the transmitted beams as marked with the black box in Fig.23. The breakup can be seen more clearly in Fig.24, where the normal holes without separating the ions with different dipole moments are used. *Ref* [18] gives sophisticated discussion for these effects. Here we introduce a simple and qualitative interpretation:

By Fourier Transform, the pulses with different time durations can be transferred to pulses with different spectral half-width FWHM. Since the passband of the hole does not cover all the frequency range of the pulse, the tail outside the hole will be absorbed and thus lost in the hole as shown in Fig.25. As shown in Fig.23 and Fig.24, with the same

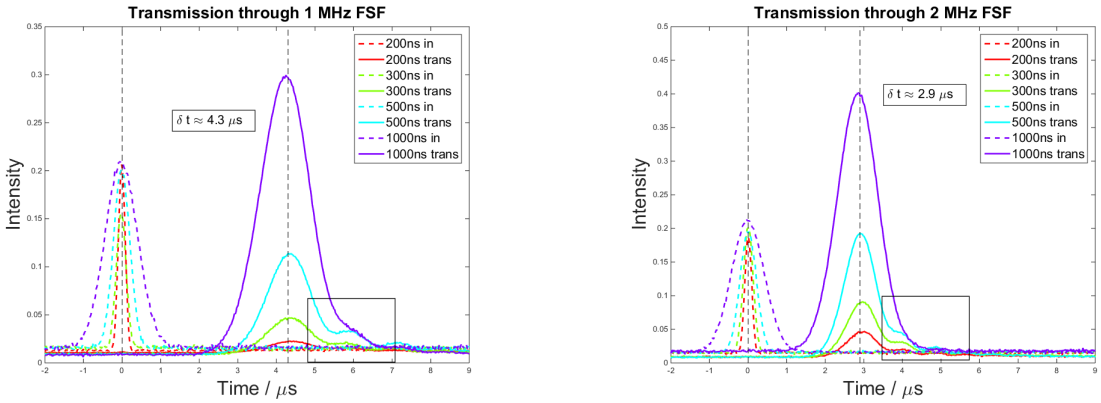

Figure 23: The time dependence of the intensity of the input beam (dots) and the transmitted beam (solid line) with different pulse duration as listed in the legend. The pulse is slowed down for 4.3 μs for the 1 MHz FSF and 2.9 μs for the 2 MHz FSF. The breakup for the transmitted beam is marked with a black box.

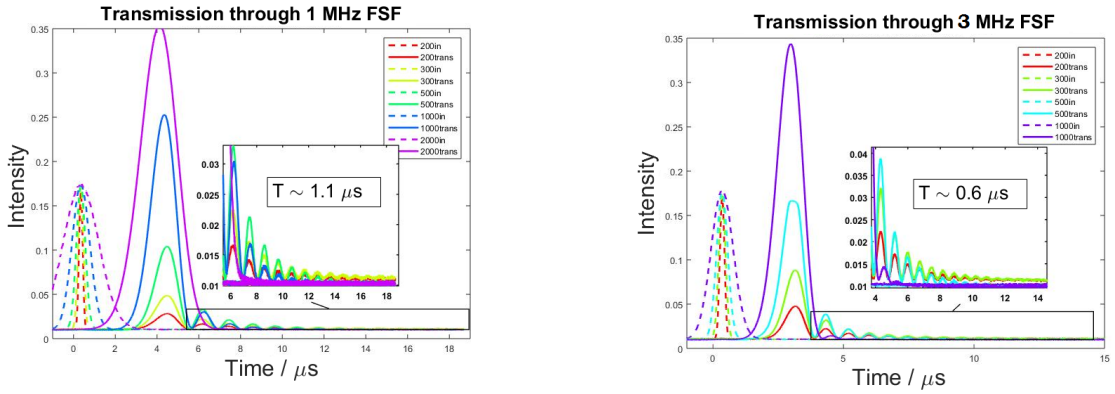

Figure 24: The breakup of transmitted beam is zoomed in. Instead of FSF, normal holes with 1 MHz and 3 MHz passband are used for higher on-off ratio of absorption inside-outside of the hole. The period of the breakup pattern is around 1.1 μs for the 1 MHz hole and 0.6 μs for the 3 MHz hole. The notations are same as in Fig.23.

incoming intensity, the intensity of the transmitted beam is higher if longer pulse is used. That is because the Fourier width of such pulse is narrower in frequency, so that the frequency component outside the hole is smaller, *i.e.* less absorption. Furthermore, as the absorption coefficient αL outside the hole is higher for the normal hole in Fig.24 than the FSF in Fig.23, more absorption will happen. The breakup pattern can be interpreted as the spontaneous decay of the ions that have been excited by the tail of the pulse outside the hole. The two parts of the tail at each side of the hole have the frequency difference slightly more than the width of the hole, and this will lead to a beating pattern. As shown in Fig.24, the period of the beating of the breakup is longer for narrower hole.

Moreover, acoording to Eq.33, the energy density distribution of the light in the FSF can be given by

$$\frac{W_{med}}{W_{vac}} = \frac{c}{n \cdot v_g} + 1. \tag{35}$$

Compared with the slow down factor $S = c/v_g$ who has the order of 10^4 to 10^5, the $+1$ and the variance of $n(\omega)$ are negligible. So the W_{med}/W_{vac} can be approximated as S assuming $n = 1$. The percentage of the energy density stored in the medium W_{med}/W_{total},

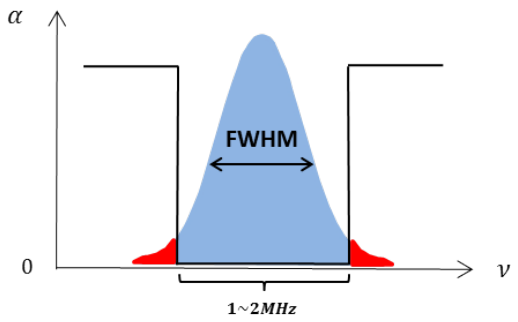

Figure 25: In frequency domain, the passband of the hole does not cover the whole pulse. The tail (marked red) outside the hole will be absorbed and the transmission will then decrease.

the slow down factor $S = c/v_g$ and the time delay δt for the two FSFs are listed in Table 5. The data taken here is given by the pulse with the spectral FWHM same as half of the FSF's passband.

Table 5: The time delay δt, slow down factor $S = c/v_g$ and percentage of the energy density stored in the medium W_{med}/W_{total} for the two FSFs with 1 MHz and 2 MHz passband.

Hole Width	δt	$S = c/v_g$	W_{med}/W_{total}
$1\ MHz$	$4.3\ \mu s$	1.3×10^5	99.9992 %
$2\ MHz$	$2.9\ \mu s$	8.7×10^4	99.9989 %

6.3.3 Frequency shift of the FSF

The frequency shift of the FSF has been tested for the 1 MHz FSF. The results for the frequency shift of the passband and the light pulse and the switch-on time of the FSF are given and discussed in this section.

Frequency shift of the passband The hole structures are read out when different electric fields are applied as in Fig.26. It can be seen that the center of the holes is shifted with the applied fields accordingly. Since there are two groups of ions outside the pit, one of them will be shifting oppositely as the hole, thus introducing absorption when the shift is too large. For a 1 MHz hole burnt in the center of an 18 MHz pit, the maximum frequency shift for the hole center is 4.75 MHz. However, as it is shown in Fig.26, the hole starts to be compressed when the frequency shift is about 4 MHz. This mainly comes from the absorption spectrum tail of the other group of ions outside the pit which has been shifted towards the hole. As discussed in Sec.5.3.2, the inhomogeneity of the electric field will also introduce absorption to the hole. For $E < E_{aver}$, where E_{aver} is the average electric field in the crystal, the absorption will be introduced from the frequency towards which the hole shifts and *visa versa* for $E > E_{aver}$. Since the absorption coefficient of the crystal is quite large, the hole is very sensitive to the introduced absorption. As shown in Fig.15b, $|E_{min} - E_{aver}| > |E_{max} - E_{aver}|$, so the hole will be more compressed from the frequency towards which it shifts. Since the absorption introduced by the other group of ions only compresses the hole from the frequency towards which it shifts as well, the hole will be more distorted at that edge.

When shifting towards the higher frequency, the right side of the hole will be more distorted, so the frequency shift of the hole is taken from the left edge of the hole. Similarly

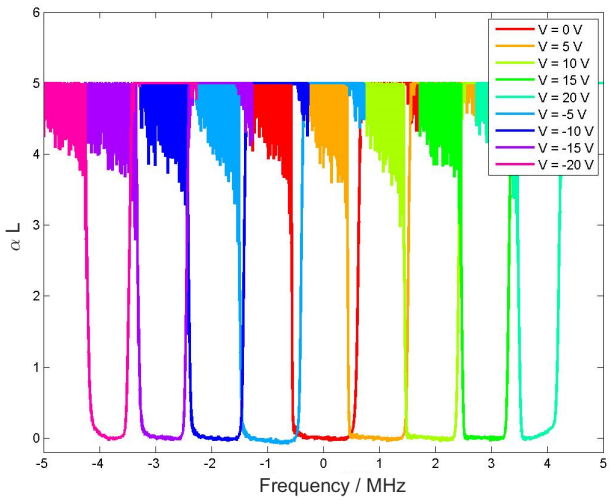

Figure 26: The hole structure of the 1 MHz FSF with different applied electric field. The line color is different for different applied voltages (from -20 V to 20 V with step of 5 V) as listed in the legend.

for the holes shifting towards the lower frequency, the frequency of the right edge is taken to calculate the frequency shifts. The frequency shifts of the hole with different applied voltages V_{app} are listed in Table 6 and plotted in Fig.27.

Table 6: The frequency shift of the hole with different applied voltage.

Applied Voltage [V]	-20	-15	-10	-5	0	5	10	15	20
Frequency shift [MHz]	-4.02	-3.02	-2.02	-1.02	0	1.00	2.01	3.02	4.02

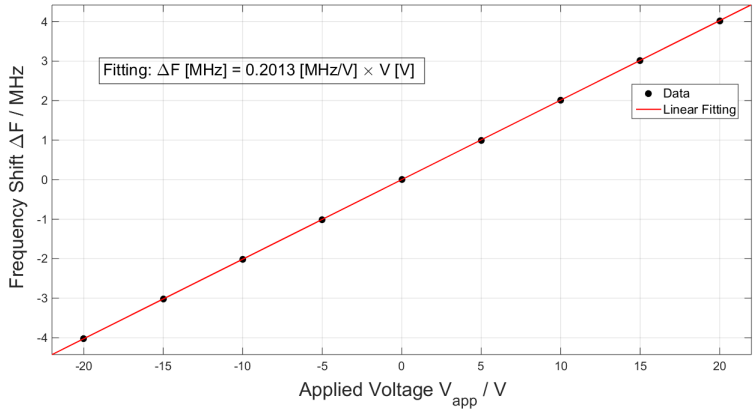

Figure 27: The frequency shift ΔF of the hole dependent on the applied voltage. The linear fitting gives ΔF [MHz] = 0.2013 [MHz/V] $\times$ V_{app} [V] with $R^2 = 0.9999$.

As shown in Fig.27, the frequency shift is proportional to the applied voltage by the linear fitting: ΔF [MHz] = 0.2013 [MHz/V] $\times$ V_{app} [V] with the coefficient of determination $R^2 = 0.9999$. Since the height of the crystal is measured as 6.3 mm and the angle between b axis (same as the direction of the electric field) and the dipole moment is given as 12.4° as in Fig.4b, the electric field dependence of the frequency shift can be given as

$$\Delta F = 129.8 \text{ kHz}/(\text{V} \cdot \text{cm}^{-1}) \frac{\delta \boldsymbol{\mu}}{|\delta \boldsymbol{\mu}|} \cdot \boldsymbol{E},$$

where the calculated gradient 129.8 kHz/(V·cm^{-1}) is the magnitude of the dipole moment.

Frequency shift of the pulse After the FSF has been prepared, a 1 μs Gaussian pulse centred at 0 MHz is sent in as a probe. As discussed in Sec.6.1, to measure the frequency of the transmitted beam, another long square pulse centred at 10 MHz is sent in right after the probe beam as the local oscillator to beat with the delayed transmitted beam. The electric field can be switched on at any time by applying an voltage on the electrodes. The three signals (input beam, beating pattern and the monitor signal from the high voltage amplifier) are recorded by the oscilloscope as shown in Fig.28.

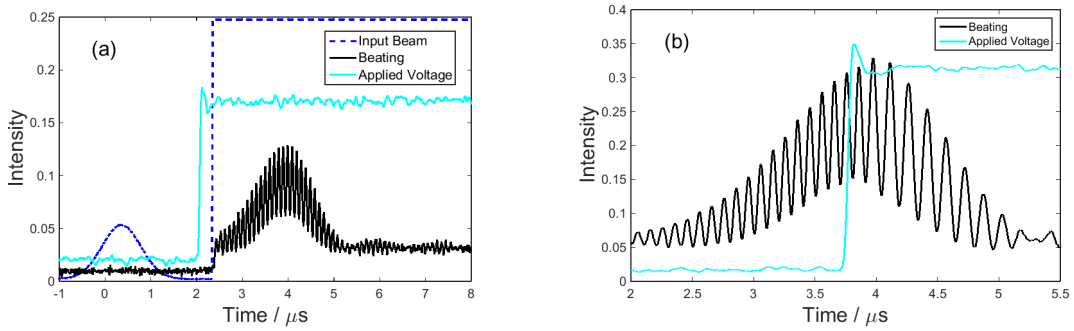

Figure 28: The time dependence of the intensity of the input beam (blue), the beating pattern (black) of the transmitted beam and the reference beam and the monitor voltage (light blue). The switch-on time and the applied voltage are different for (a) and (b) as indicated individually. For (a), the voltage is switch on when all the pulse is inside the crystal with $V_{app} = 10$ V. For (b), the voltage is switch on when half of the pulse has come out of the crystal with $V_{app} = 20$ V. The change of the beating pattern reflects that the frequency of the transmitted beam changes instantaneously with the change of the electric field.

By fast Fourier transform (FFT) of the beating pattern, the frequency shift of the transmitted beam is calculated and listed in Table 7. As plotted in Fig.29, the shift of the frequency is proportional to the applied voltage. The linear fitting gives ΔF [MHz] = 0.1778 [MHz/V]$\times V_{app}$ [V], with $R^2 = 0.9995$. Similarly as the calculation for the frequency shift of the hole, the electric field dependence of the frequency shift of the pulse is given as

$$\Delta F = 114.7 \text{ kHz/(V} \cdot \text{cm}^{-1}) \frac{\delta \boldsymbol{\mu}}{|\delta \boldsymbol{\mu}|} \cdot \boldsymbol{E},$$

where the calculated gradient 114.7 kHz/(V·cm^{-1}) is the magnitude of the dipole moment.

Table 7: The frequency shift of the pulse center with different applied voltages.

Applied Voltage [V]	-25	-20	-15	-10	-5
Frequency Shift [MHz]	-4.55	-3.62	-2.69	-1.82	-0.98
Applied Voltage [V]	25	20	15	10	5
Frequency Shift [MHz]	4.39	3.49	2.56	1.71	0.85

The magnitude of the dipole moment calculated here from the fitting of the frequency center of the pulse and applied field is smaller than the one calculated from the frequency shift of the hole. This is due to the fact that the frequency center of the frequency distribution of the transmitted pulse is asymmetric. As discussed and shown in Fig.26, when shifting towards higher/lower frequency, absorption will be introduced either because the

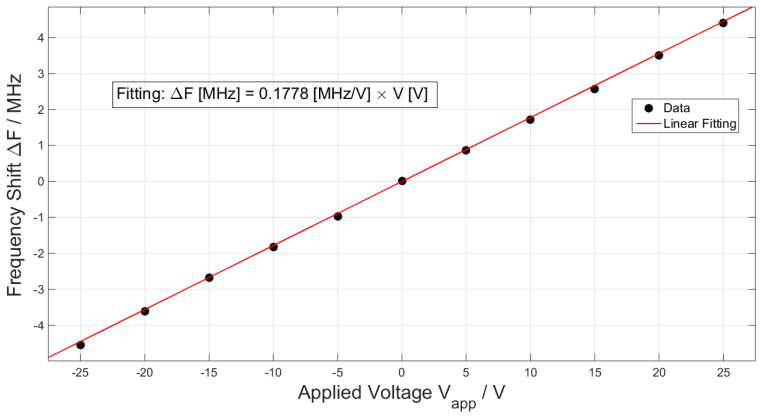

Figure 29: The frequency shift ΔF of the pulse dependent on the applied voltage. The linear fitting gives ΔF [MHz] $= 0.1778$ [MHz/V] $\times V_{app}$ [V] with $R^2 = 0.9995$.

other group of ions outside the pit that has been shifted towards to the hole or due to the inhomogeneity of the electric field. As a result, the corresponding frequency components of the transmitted pulse will be absorbed and thus lost. Since the higher/lower frequency component of the pulse will be more absorbed when shifting towards the higher/lower frequency as shown in Fig.30, the frequency distribution of the pulse will thus become asymmetric. As a result, the frequency shift of the pulse center will be smaller and also the magnitude of the dipole moment calculated from it will be smaller than it calculated from the undistorted edge of the hole.

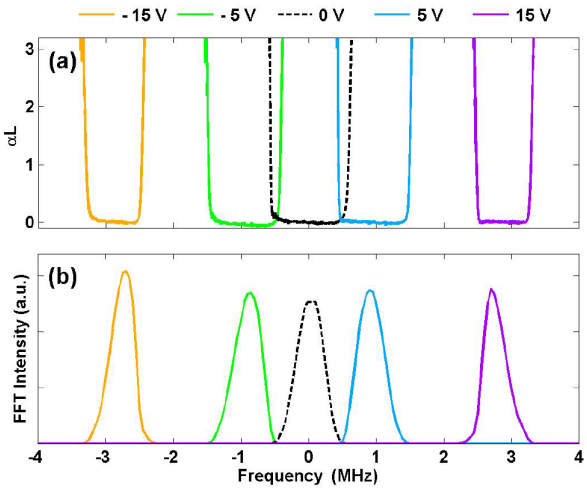

Figure 30: The hole structure (a) and the frequency distribution of the transmitted pulse (b) with different applied voltages. The hole will be compressed because of the absorption introduced either by the absorption spectrum tail of the other group of ions outside the pit or due to the inhomogeneity of the electric field as discussed in Sec.5.3.2. The frequency component of the transmitted pulse will be lost because of the introduced absorption, and this will lead to an asymmetric frequency distribution of the pulse and a shift of the frequency center of the pulse.

As discussed above, the introduced absorption of the hole and the frequency component lost for the pulse from the frequency opposite to which the hole/pulse shifts towards can only be caused by the inhomogeneity of the field. As shown in Fig.30, this part of both the hole and pulse retains its shape quite well. It could be interpreted as if the inhomogeneity of the field has little effect on the hole structure and pulse reshaping.

The switch-on time of the FSF The beating pattern in Fig.28b shows that the frequency of the transmitted beam changes immediately as the voltage is applied. It is more clearly shown in Fig.31 where the instantaneous frequency of the transmitted beam and the applied voltage are compared. As shown in Fig.31, the frequency shift of the transmitted beam follows the applied voltage with a delay of about 40 ns. However, the switch-on time of the FSF is further limited by the rise time of the electric field. In this case, the switch-on time of the FSF is about 200 ns.

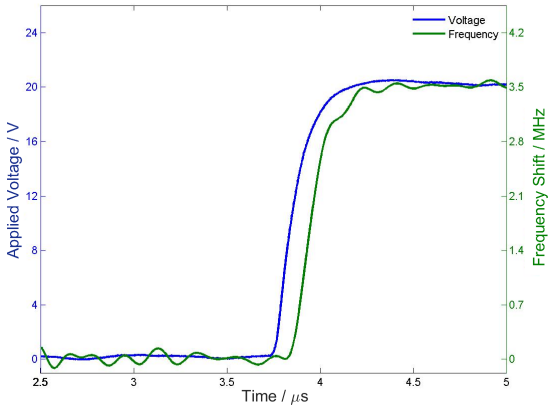

Figure 31: The time dependence of the frequency shift of the transmitted beam and the applied voltage. The frequency shift follows the applied voltage well with a delay of about 40 ns.

7 Ultrasound Optical Tomography

In this section, the Ultrasound Optical Tomography (UOT), the initial motivation for the development of the FSF, will be discussed. It will show that the FSF could be the deal-breaker for the practical use of the UOT.

Ultrasound Optical Tomography is a medical imaging method used to detect the tissue deep inside the body with high resolution and high contrast. While optical imaging has superior sensitivity to provide information about the chemical properties of the texture, its resolution is highly degraded by the scattering in the material. This becomes a problem when observing a strongly scattering material, *e.g.* breast tumours. Ultrasound imaging, on the contrary, can give high resolution for such diffuse materials, but is not sensitive enough to provide chemical information of the texture. The UOT, as a combination of the two methods, was proposed as a new approach for human tissue imaging that has both the high sensitivity of optical imaging and the high resolution of ultrasound imaging [1].

Inside the tissue, the ultrasound works as a grating for the probe light. If and only if the light propagates through the ultrasound pulse which can be focussed to less than a mm^3, two side-bands shifted from the original laser frequency ν_l by +/- the ultrasound frequency ν_{us} will be created. The light passing through such region will thus be tagged by the ultrasound. When there is an absorber, *e.g.* a tumour, at the ultrasound focus, light will be absorbed and no side-bands are created. So the information of the focus region can be given by detecting the side-bands, which will be referred to as the *UOT signal* in the rest of the thesis. However, since only a very small portion of the probe laser goes through the ultrasound focus, the intensity of the UOT signal can be of the order of 60 dB below the non-frequency-shifted light [2]. This makes UOT not being able to be used practically.

Recently, it has been found that the slow light effect occurring in the spectral filter can significantly improve the performance for UOT [3]. An optimised UOT combined with spectral filters was thus proposed [2]. A schematic illustration of the set-up is shown in Fig.32a. The UOT signal is amplified similarly as in a laser cavity. Since the left and right chains are identical, a detailed illustration of the right chain is given to show how this scheme works as in Fig.32b.

Similarly as for a laser, the gain media is used to overcome the losses of the UOT signal when propagating through the tissue. Since all other light frequencies will be filtered out, it is only the UOT signal that has been reflected to its incident path, *i.e.* this one always goes through the ultrasound focus, that will be able to oscillate and be amplified in the cavity. As mentioned before, the UOT signal is much weaker than the probe laser and to limit the gain required to overcome the losses, a phase conjugated mirror [28] is used. Unlike a normal mirror that can only reflect the incoming beam to its incident path when the incident angle is 90 degree, the phase conjugated mirror can reflect the incoming beam to its incident path with a 2π acceptance angle. When the gain is larger than the losses in the tissue, it will work as a laser, and the UOT signal will be amplified. Moreover, since the laser has the "winner takes all" mechanism, it is the UOT signal that takes the shortest route in the tissue or least absorbed in the tissue, that will be chosen and amplified. This will automatically avoid the high loss regions, *e.g.* blood vessel, which would absorb the light and prevent imaging at large depths.

The rest of the components, *i.e.* the FSFs, are used to select the UOT signal from the non-frequency-shifted light and change the frequency of the UOT signal. The filter has

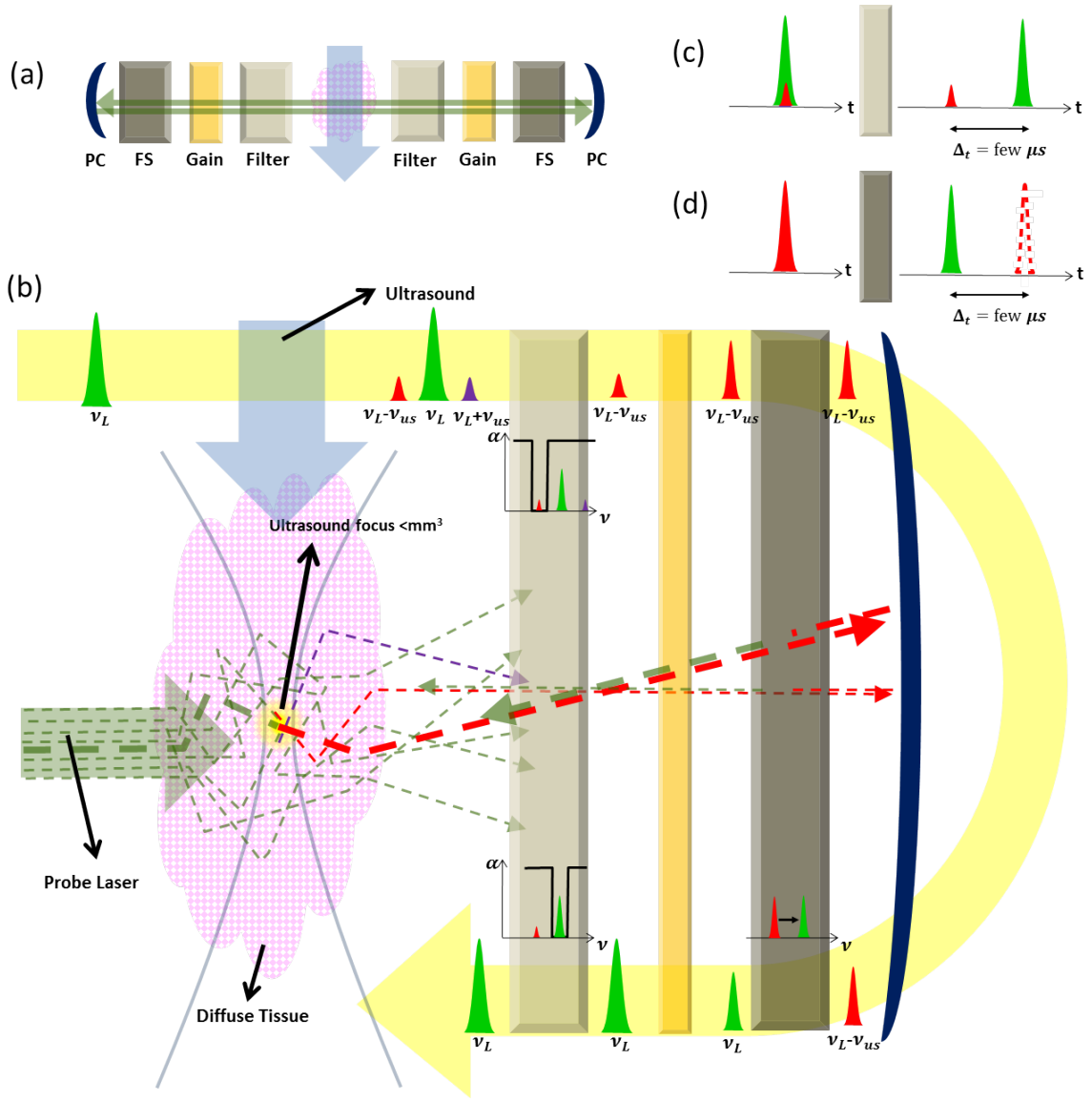

Figure 32: An illustration of the optimised UOT: (a) The UOT works as a laser cavity containing two identical chains with filters, gain media, frequency shifters (FS), and phase conjugators (PC). The UOT signal will oscillate and be amplified in the cavity. (b) A detailed illustration for one chain: The dashed arrows with different colors represent light with different frequencies (green for μ_l, red for $\mu_l - \mu_{us}$ and purple for $\mu_l + \mu_{us}$). The frequency change of the UOT signal in the cavity through each components is presented as guided by the yellow arrow. The light passing through the ultrasound focus will be shifted by +/- ν_{us}; the filter has the passband for the UOT signal from one side-band (the one with lower frequency is chosen here) and only this UOT signal can pass through and be amplified; the FS will shift the UOT signal back to ν_l after it has been reflected by the PC; the PC can reflect the signal back to its incident path with a 2π acceptance angle for light; and the gain medium is used to overcome the losses of the UOT signal in the tissue and rest of the cavity. (c) The UOT signal will be delayed for several μs after passing through the filter to increase the signal-noise-ratio. (d) The FS will delay the UOT signal for several μs to provide the time for the filter to change its passband.

the passband for one of the two side-bands while the non-shifted light and the other side-band light will be absorbed. It is equivalent to choosing either one of the side-bands. In Fig.32b, the side-band with lower frequency (marked red) is chosen. As mentioned before, the slow light effect will occur when light passing through such a filter. As a result, the UOT signal will be delayed for several μs as shown in Fig.32c. This will separate the UOT

signal and the background signal that has not been completely absorbed by the filter, thus improving the signal-to-noise ratio and the performance of the UOT. As the UOT signal is not much stronger than the background signal, this could be the deal-breaker for the practical use of UOT.

When oscillating in the cavity, the UOT signal will pass through the ultrasound focus many times. Whenever it passes through it, its frequency will be shifted ν_{us} further from ν_l. Although it in principle could be solved by changing the passband of filter accordingly, it is not only unrealistic, but also not wise to do so since the frequency of the detected signal can not be fixed either. To overcome this problem, a frequency shifter (FS) which can shift the frequency of the UOT signal to its original frequency ν_l is added. The shift of the frequency happens when the UOT signal passes through the FS after being reflected by the PC. Meanwhile, the passband of filter should be changed to ν_l so that the shifted-to-original UOT signal can pass through it. The slow light effect in the FS, as shown in Fig.32d, will provide the time for the filter to shift its passband. The frequency change of the UOT signal in the cavity through each components is presented in Fig.32b guided by a yellow arrow. It will be shifted to ν_l each time before passing through the tissue and shifted to $\nu_l + \nu_{us}$ by the ultrasound when passing through the ultrasound focus in the tissue.

In conclusion, the filter should be able to (1) have tunable passband, (2) delay the UOT signal that propagates in the passband and (3) have 2π acceptance angle for the light, while the FS should be able to (1) shift the frequency of the UOT signal, (2) delay the UOT signal, and (3) have 2π acceptance angle for the light. All the requirements for both the filter and the FS can be satisfied with one FSF developed in this thesis!

8 Outlook

In conclusion, for the purpose of designing and testing an FSF, the experiment is quite successful. For a 1 $\sim$ 2 MHz FSF, the light can be slowed down to $c/10^4 \sim c/10^5$. For a 1 MHz FSF, the frequency shift of -4 to 4 MHz for both the passband and the light pulse is clearly observed. The linear fitting of the frequency shift of the passband, ΔF [MHz] = 0.2013 [MHz/V] $\times$ V_{app} [V] with $R^2 = 0.9999$, gives the magnitude of the dipole moments as 129.8 kHz/(V$\cdot$cm^{-1}). The switch-on time of the FSF is around 200 ns, limited by the rise time of the electric field. However, when testing the FSF, although the frequency-shifted light pulse is clearly observed, the efficiency of the FSF is not measured. It could be simply given by measuring the intensity of the light before passing through the FSF.

In this project, the frequency shift of the pulse is limited by half of the pit width. However, larger frequency shift could be achieved with the similar spectral structure as long as the hole is not filled with absorption when applying the electric field. The absorption, as discussed in Sec.6.3, is introduced mainly by the other group of ions which shift towards the opposite frequency as the hole. This absorption will not be a problem when the hole is shifted out of the inhomogeneous profile of the other group of ions as shown in Fig.33a. When the frequency shift is not that large, the absorption could also be

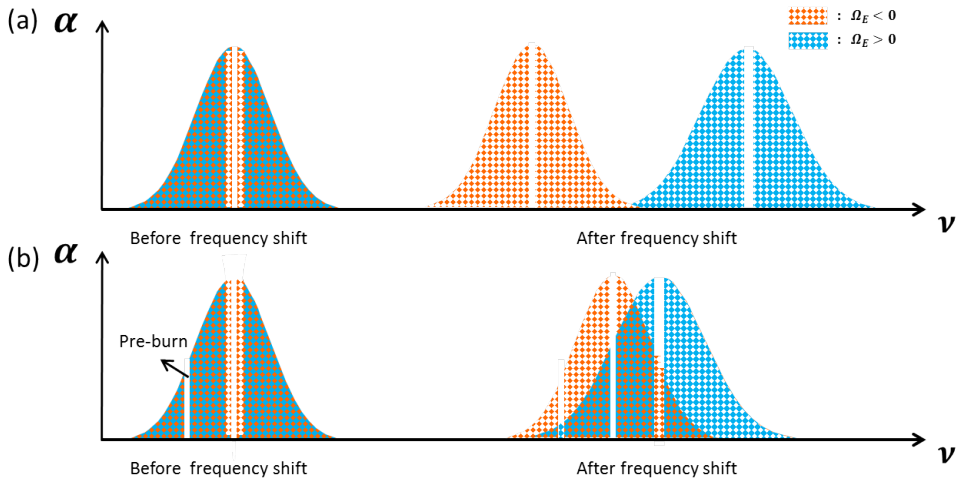

Figure 33: (a) When the hole is shifted out of the inhomogeneous profile of the other group of ions, no absorption will be introduced. (b) When the frequency shift is not that large, the absorption could be avoided by pre-burning a hole before the frequency shift.

avoided by pre-burning a hole at the frequency who will be shifted to the FSF's passband when applying the electric field as shown in Fig.33b. The frequency shift of the FSF will thus only be limited by the breakdown voltage of the crystal. For the REE doped crystal, its breakdown voltage could be as high as few MV/cm, which will allow the frequency shift of a few hundred GHz.

Furthermore, other interesting experiments could also be done using the spectral hole-burning technique on rare-earth-doped crystal and external electrical field. Here an example is given: when applying an electric field on a normal hole surrounded by both groups of ions with different dipole moment orientations, the hole will be compressed as shown in Fig.34. The change of the spectral structure, *i.e.* the hole width, will lead to the change of the refractive index and $\partial n/\partial\omega$. Since the group velocity of the pulse

propagating through the hole is closely related to $\partial n/\partial\omega$, it will be possible to control the group velocity of the pulse by the magnitude of the applied electric field.

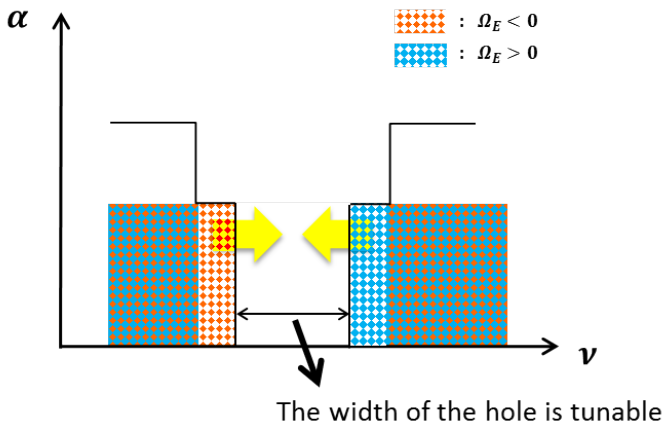

Figure 34: The spectral structure of a hole with tunable width. When applying an electric field, the hole will be compressed because of the opposite shift of the two groups of ions. The change of the spectral structure leads to the change of the refractive index who is closely related to the group velocity of the light passing through the hole. As a result, the group velocity will be controlled by the magnitude of the applied field.

Appendices

A Crystal Coating

A.1 Crystal Coating contract

Mariusz.Graczyk@ftf.lth.se 2015-06-24

Contact evaporation on Y2SiO5 crystal for Yupan Bao

Materials;
Substrate holder for shadow evaporation
Crystal Y2SiO5 10x10x6mm sample 2-589-04
(0.05% PrYSO from Scientific Materials Co.)
Ti
Au
Acetone and IPA for cleaning

Procedure;

1. Crystal cleaning
   Acetone 30ml on HP 80°C 5min - crystal in vertical position (cleaning contact surfaces)
   Acetone 30ml ultrasonic 5min - crystal in vertical position (cleaning contact surfaces)
   IPA 30ml on HP 80°C 5min - crystal in vertical position (cleaning contact surfaces)
   IPA 30ml ultrasonic 5min - crystal in vertical position (cleaning contact surfaces)
   Blow dry with N2
2. Evaporation
   Place crystal in the holder, longer side 10.16mm is perpendicular to the gap in the evaporated contact – crystal direction is important!

   Evaporate in Pfeiffer – first (top) contact
   Base pressure 1*10-7mbar (night pumping)
   Ti rate around 1Å/s, thickness 50Å, manual evaporation
   Au rate 10Å/s, thickness 2000Å, automatic evaporation
   Ventilate, open and reload sample and material
   Evaporate in Pfeiffer – second (bottom) contact
   Base pressure 4.8*10-7mbar (3 h time slot, day time)
   Ti rate around 1Å/s, thickness 50Å, manual evaporation
   Au rate 10Å/s, thickness 2000Å, automatic evaporation

A.2 *Solidwork* drawings of the mask

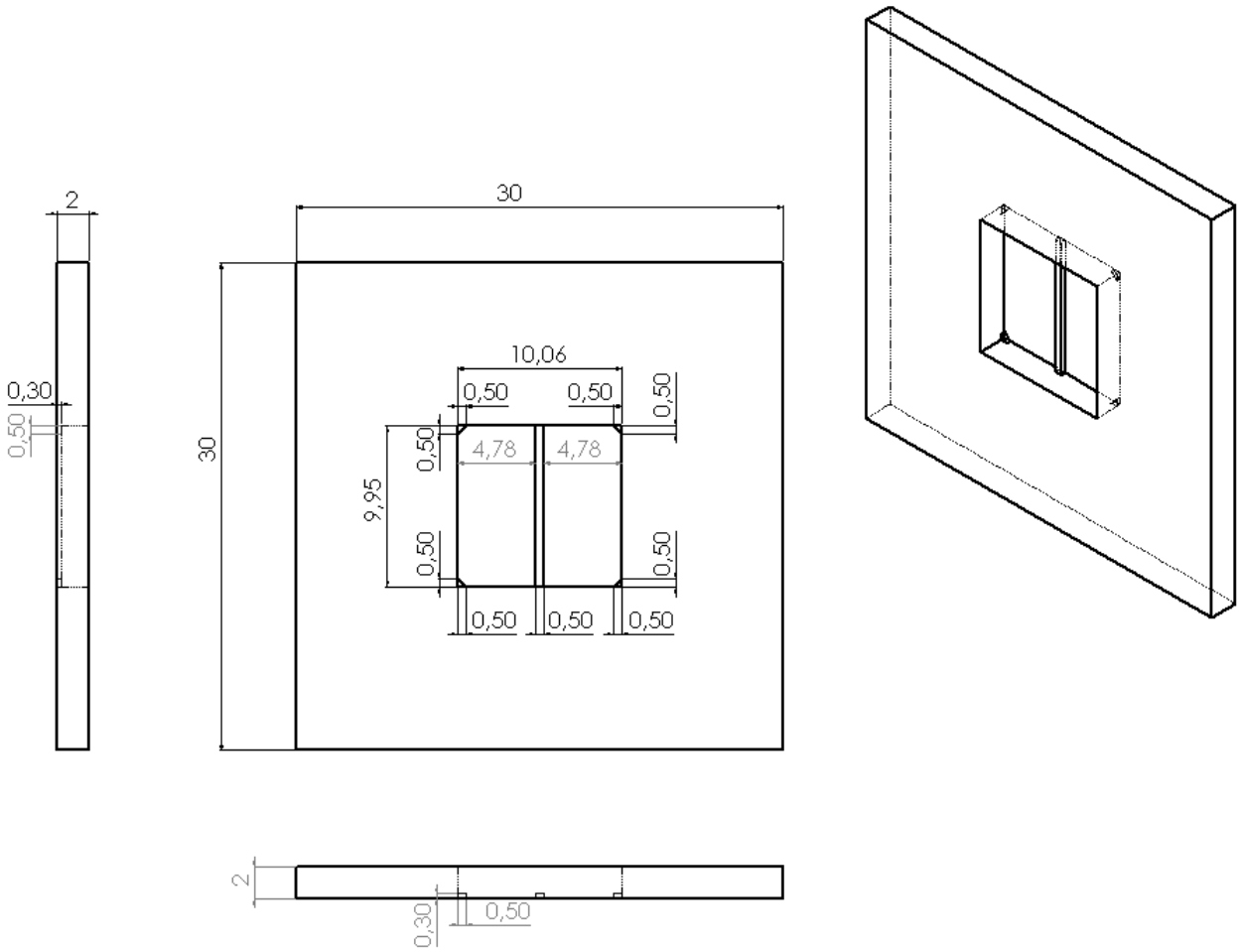

References

[1] Fay A Marks, Harold W Tomlinson, and Glen W Brooksby. Comprehensive approach to breast cancer detection using light: photon localization by ultrasound modulation and tissue characterization by spectral discrimination. In *OE/LASE'93: Optics, Electro-Optics, & Laser Applications in Science& Engineering*, pages 500–510. International Society for Optics and Photonics, 1993.

[2] Private communication with Stefan Kröll. A proposal for slow light applications and materials. .

[3] Huiliang Zhang, Mahmood Sabooni, Lars Rippe, Chulhong Kim, Stefan Kröll, Lihong V Wang, and Philip R Hemmer. Slow light for deep tissue imaging with ultrasound modulation. *Applied physics letters*, 100(13):131102, 2012.

[4] Inc. Comsol. Comsol multiphysics modeling software, Retrieved 20 November 2015.

[5] Gordon B. Haxel, James B. Hedrick, Greta J. Orris, Peter H. Stauffer, and James W. Hendley II. Rare earth elements: critical resources for high technology. Technical report, 2002. Report.

[6] Mahmood Sabooni. *Efficient Quantum Memories Based on Spectral Engineering of Rare-Earth-Ion-Doped Solids*. PhD thesis, Lund University, 2013.

[7] R. W. Equall, R. L. Cone, and R. M. Macfarlane. Homogeneous broadening and hyperfine structure of optical transitions in pr^{3+}:y_2sio_5. *Phys. Rev. B*, 52:3963–3969, Aug 1995.

[8] Mattias Nilsson. *Coherent Interactions in Rare-Earth-Ion-Doped Crystal for Applications in Quantum Information Science*. PhD thesis, Lund University, 2004.

[9] Jenny Karlsson. *Cerium as a quantum state probe for rare-earth qubits in a crystal*. PhD thesis, Lund University, 2015.

[10] Mattias Nilsson, Lars Rippe, Stefan Kröll, Robert Klieber, and Dieter Suter. Hole-burning techniques for isolation and study of individual hyperfine transitions in inhomogeneously broadened solids demonstrated in pr^{3+}: Y_2sio_5. *Phys. Rev. B*, 70:214116, Dec 2004.

[11] BA Maksimov, VV Ilyukhin, Yu A Kharitonov, and NV Belov. The crystal structure of y 2 o 3. sio 2= y 2 sio 5 yttrium oxiorthosilicate the dual function of yttrium. 1970.

[12] Felix R. Graf, Alois Renn, Urs P. Wild, and Masaharu Mitsunaga. Site interference in stark-modulated photon echoes. *Phys. Rev. B*, 55:11225–11229, May 1997.

[13] Jacob B. Khurgin. Slow light in various media: a tutorial. *Adv. Opt. Photon.*, 2(3):287–318, Sep 2010.

[14] *Classical Electrodynamics (3rd Edition)*, chapter 7.5. Wiley, 2004.

[15] Matthew Borenstein and Willis E. Lamb. Effect of velocity-changing collisions on the output of a gas laser. *Phys. Rev. A*, 5:1311–1323, Mar 1972.

[16] R. de L. Kronig. On the theory of dispersion of x-rays. *J. Opt. Soc. Am.*, 12(6):547–557, Jun 1926.

[17] C. G. B. Garrett and D. E. McCumber. Propagation of a gaussian light pulse through an anomalous dispersion medium. *Phys. Rev. A*, 1:305–313, Feb 1970.

[18] R. N. Shakhmuratov and J. Odeurs. Off-resonance slow light. *Phys. Rev. A*, 78:063836, Dec 2008.

[19] R.N. Shakhmuratov. The energy storage in the formation of slow light. *Journal of Modern Optics*, 57(14-15):1355–1365, 2010.

[20] Eric Courtens. Giant faraday rotations in self-induced transparency. *Phys. Rev. Lett.*, 21:3–5, Jul 1968.

[21] RM Macfarlane and RM Shelby. Photoionization hole burning and nonlinear zeeman effect in caf 2: Sm 2+. *Optics letters*, 9(12):533–535, 1984.

[22] AA Gorokhovskii, RK Kaarli, and LA Rebane. Hole burning in the contour of a pure electronic line in a shpolskii system. *JETP Lett*, 20(7):474–497, 1974.

[23] Keith Holliday, Mauro Croci, Eric Vauthey, and Urs P Wild. Spectral hole burning and holography in an y 2 sio 5: Pr 3+ crystal. *Physical Review B*, 47(22):14741, 1993.

[24] Akash Yadav and Lalit Gupta. Developing and testing a set-up for controlling the absorption frequency of rare earth ions in an inorganic crystal, 2013.

[25] C Blank and MH Edwards. Dielectric breakdown of liquid helium. *Physical Review*, 119(1):50, 1960.

[26] A. Amari, A. Walther, M. Sabooni, M. Huang, S. Krll, M. Afzelius, I. Usmani, B. Lauritzen, N. Sangouard, H. de Riedmatten, and N. Gisin. Towards an efficient atomic frequency comb quantum memory. *Journal of Luminescence*, 130(9):1579 – 1585, 2010. Special Issue based on the Proceedings of the Tenth International Meeting on Hole Burning, Single Molecule, and Related Spectroscopies: Science and Applications (HBSM 2009) - Issue dedicated to Ivan Lorgere and Oliver Guillot-Noel.

[27] Philip Dalsbecker. Development of narrow-bandwidth filters for the suppression of scattered light for optical and ultrasound analysis of tissue. Master's thesis, Lund University, 2015.

[28] *Fundamentals of Photonics (Second Edition)*, chapter 21.3.E. Wiley, 2007.